

The ionised interstellar medium of DSFGs revealed by JWST/NIRSpec and ALMA: Super-solar metallicity, low ionisation parameters and, typical electron densities

Steven Gillman,^{1,2} Kei Ito,^{1,2} Francesco Valentino,^{1,2} Gabe Brammer,^{1,3} Pablo Araya Araya,^{1,2} Georgios Magdis,^{1,2} Ugnė Dudzevičiūtė,^{1,2} Aswin P. Vijayan,⁴ Minju Lee,^{1,2} Bitten Gullberg,^{1,2} Daniel Ceverino,^{5,6} Andreas L. Faisst,⁷ Seiji Fujimoto,^{8,9} Thomas R. Greve,^{1,2} Rashmi Gottumukkala,^{1,3} Chandana Hegde,^{1,2} Michaela Hirschmann,¹⁰ Shuowen Jin,^{1,2} Christian Kragh Jespersen,¹¹ Takumi Kakimoto,^{12,13} Mariko Kubo,^{14,15} Peter Laursen,^{1,3} Masato Onodera,^{12,16} Antonio Pensabene,^{1,2} Francesca Rizzo,¹⁷ John R. Weaver,¹⁸ Po-Feng Wu,^{19,20}

(Affiliations can be found after the references)

February 24, 2026

ABSTRACT

We present a detailed study of the observed-frame near-infrared (2–4 μm) JWST/NIRSpec spectra of 48 high-redshift ($z = 2.53_{-0.70}^{+1.32}$) galaxies detected with ALMA at $>3\sigma$. Through a multi-wavelength SED analysis we establish the sample has a median stellar mass of $\log_{10}(M_*[M_\odot]) = 10.8 \pm 0.1$ and dust mass of $\log_{10}(M_d[M_\odot]) = 8.7 \pm 0.1$, covering a broad range of far-infrared luminosity ($\log_{10}(L_{\text{FIR}}[L_\odot]) = 10.9 - 12.7$). Analysing the rest-frame optical emission-line properties, we discern the majority of the sources show no indication of AGN activity with 40% having either X-ray counterparts ($L_{\text{Xc}} > 10^{42}$ erg/s), elevated optical ($[\text{OIII}]/\text{H}\beta$, $[\text{NII}]/\text{H}\alpha$) emission-line ratios or broad (FWHM > 800 km/s) $\text{H}\alpha$ emission line profiles, although we note this is a lower limit given the stochastic placement of NIRSpec slits. We establish the sample has a median gas-phase metallicity of $12 + \log_{10}(\text{O}/\text{H}) = 8.71 \pm 0.02$, as derived from the $[\text{NII}]/\text{H}\alpha$ ratio, with the more far-infrared luminous ($\log_{10}(L_{\text{FIR}}[L_\odot]) > 12.0$) galaxies exhibiting 0.15 ± 0.03 dex higher metallicity at their epoch than predicted by the fundamental metallicity relation. From the $[\text{SII}]$ emission-line doublet ratio, we measure a median electron density for the sample of $\log_{10}(n_e[\text{cm}^{-3}]) = 2.53 \pm 0.07$, consistent with less-massive, star-forming, galaxies at the same epoch. Finally, for a subsample of nine sources with $[\text{OII}]$ and $\text{H}\beta$ detections (median $\log_{10}(L_{\text{FIR}}[L_\odot]) = 11.81 \pm 0.15$), we derive a median observed (dust-uncorrected) ionisation parameter of $\log_{10}(U) = -2.84 \pm 0.06$, suggesting our sample fall below the ionisation parameter $\text{H}\alpha$ star-formation rate surface density ($\Sigma_{\text{H}\alpha, \text{SFR}}$) relation of typical star-forming galaxies. Our results indicate that luminous far-infrared galaxies are massive, chemically evolved, systems that appear to deviate from the standard dust and metal production equilibrium observed in less obscured galaxies. This study demonstrates the powerful synergy of JWST and ALMA in unveiling the nature of dusty star-forming galaxies, and highlights the need for a NIRSpec survey of uniformly selected, massive, dust obscured, galaxies to fully characterise their interstellar medium.

Key words. Galaxies: high-redshift – Galaxies: evolution – Galaxies: ISM – Sub-millimetre: galaxies

1. Introduction

In the last few decades, large photometric surveys have revealed that up to 70% of the co-moving star formation rate density at $0.5 < z < 4$ is obscured by dust (e.g. Chary & Elbaz 2001; Schreiber et al. 2015), with this fraction declining at higher redshifts (e.g. Algera et al. 2023; Martis et al. 2025). At Cosmic Noon ($z \approx 1-4$) the most extreme examples of galaxies with heavily obscured emission are sub-millimetre bright galaxies (SMGs) (e.g. Blain et al. 2002; Casey et al. 2014; Dudzevičiūtė et al. 2020; Simpson et al. 2020; Liao et al. 2024) but there are also significant contributions from fainter (< 1 mJy) sub-millimetre galaxies (e.g. Cowie et al. 2002; Clements et al. 2008; Fujimoto et al. 2016; Aravena et al. 2016; Suzuki et al. 2021), that together are collectively known as dusty star-forming galaxies (DSFGs). For a full review see Casey et al. (2014).

The high star formation rates ($\text{SFR} \sim 10^{2-3} M_\odot \text{yr}^{-1}$) and large stellar masses ($> 10^{10} M_\odot$) of DSFGs has proved challenging to reproduce in theoretical galaxy formation models (e.g., Baugh et al. 2005; Swinbank et al. 2008; Hayward et al. 2013; McAlpine et al. 2019), although more recent attempts have been

more successful (e.g., Lovell et al. 2022; Lower et al. 2023; Cochrane et al. 2024). The models suggest that the high star formation rates in this population are driven by a mix of secular instabilities in gas-rich discs and dynamical triggers due to minor and major mergers (e.g., McAlpine et al. 2019).

However, in contrast high-resolution observational studies of the dust continuum in DSFGs (e.g., Simpson et al. 2015; Ikarashi et al. 2015; Fujimoto et al. 2017) has revealed compact disk-like structures (i.e., $R_e \sim 1-2$ kpc, Sérsic $n \approx 1$) as well as evidence for a fainter more extended component with $R_e \approx 4$ kpc (e.g., Gullberg et al. 2019; Ivison et al. 2020). In addition, resolved kinematic studies using molecular and atomic fine structure emission lines in the rest-frame far-infrared and sub-/millimetre have uncovered disk-like kinematics for at least a significant fraction of the population (e.g., Hodge et al. 2012; Chen et al. 2017; Lelli et al. 2021; Rizzo et al. 2021; Amvrosiadis et al. 2023). More recent high resolution studies with JWST have further revealed remarkably uniform, disc-dominated, morphologies at rest-frame near-infrared (1 μm) wavelengths (e.g. Gillman et al. 2024; McKinney et al. 2024; Bodansky et al. 2025), with only the most extreme, high redshift ($z > 3$) DSFGs, show-

ing high fractions of mergers and interactions (e.g. Hodge et al. 2025). This suggests for the bulk of the DSFG population, their evolution is secularly driven and not dominated by major mergers as previously suggested.

This raises the question then what is driving the extreme, dust-obscured, often star-bursting, nature in high-redshift DSFGs, given their apparent secular (i.e. non-major merger) dominated evolution. Less dust-obscured star-forming galaxies at the same epoch, follow tight scaling relations, such as the main sequence of star formation (e.g. Speagle et al. 2014; Popesso et al. 2023), the mass metallicity relation (e.g. Tremonti et al. 2004; Sanders et al. 2021) and fundamental metallicity relation (e.g. Mannucci et al. 2010; Curti et al. 2020), that represent the equilibrium status between ongoing gas consumption and star formation, prior star-formation (stellar mass) alongside metal enrichment and dust production processes (see Förster Schreiber & Wuyts 2020 for a full review). It is often assumed that dust-obscured galaxies exhibit the same equilibrium between star-formation and dust and metal enrichment, with many studies employing the scaling relations to indirectly infer gas-phase metallicities (e.g. Liu et al. 2019; Donevski et al. 2020; Kokorev et al. 2021; Gómez-Guijarro et al. 2022). However, given the extreme nature of DSFGs, with high stellar masses and star formation rates, whether such an assumption is valid is not well defined.

Whilst constraining the stellar mass and star-formation rates, and thus relation to the main sequence of star formation, of dust-obscured galaxies has been possible for many years (e.g. Swinbank et al. 2014; Dunlop et al. 2017; Long et al. 2023), with the most heavily dust-obscured systems elevated specific star formation rates placing them in the starburst regime (e.g. Silverman et al. 2015; Dudzevičiūtė et al. 2020; Puglisi et al. 2021; Faisst et al. 2025), measuring the galaxies metallicity has remained a challenge. To constrain the metallicity of the interstellar medium we would ideally use the far-infrared fine structure lines (e.g. [O I] 63 μ m, [Si II] 34 μ m, [N III] 57 μ m), which are unaffected by dust obscuration. However, at $z < 4$, ALMA can not detect the multiple line diagnostics required (e.g. Decarli & Díaz-Santos 2025). Prior studies using the Herschel space telescope achieved detections in stacked low signal to noise spectra of the far-infrared fine structure lines (e.g. Coppin et al. 2012; Wardlow et al. 2017; Wilson et al. 2017; Rigopoulou et al. 2018a; Bakx et al. 2026) or utilised lensing (e.g. Zhang et al. 2018), to reveal on average super solar metallicities.

Another option is to use rest-frame optical lines, in combination with strong-line calibrations (e.g. Maiolino & Mannucci 2019), to derive gas-phase metallicities and other interstellar medium properties. Although, these should not be interpreted as direct equivalents of those inferred from far-infrared fine-structure lines, as the two sets of diagnostics probe gas at different characteristic densities and physical conditions (e.g. Harikane et al. 2025; Usui et al. 2025). Detecting rest-frame optical emission lines in high-redshift ($z > 1$) in dust-obscured galaxies is traditionally very challenging due to their inherent optical faintness. Limitations from ground-based instrumentation sensitivity often results in low signal to noise spectra dominated by atmospheric affects (i.e. OH skylines) with limited wavelength coverage in a subsample of the brightest, least dust-obscured, sources (e.g. Swinbank et al. 2004; Alaghband-Zadeh et al. 2012; Menéndez-Delmestre et al. 2013; Suzuki et al. 2021; Shapley et al. 2020; Hogan et al. 2021; Birkin et al. 2024a).

With the advent of JWST/NIRSpec it is now possible to detect the rest-frame optical emission lines at high-redshift in dust-obscured galaxies at high signal to noise and resolution. Early JWST studies utilised the NIRSpec/PRISM mode to reveal the

diverse rest-frame optical spectroscopic properties of a small sample of far-infrared bright galaxies (e.g. Cooper et al. 2025; Price et al. 2025), but lacked the spectroscopic resolution to resolve key line ratios, and thus infer interstellar medium properties. A more recent study by Kiyota et al. (2026) utilised medium resolution ($R \sim 1000$) NIRSpec/MSA spectroscopy from the JWST Advanced Deep Extragalactic Survey (JADES; Eisenstein et al. 2023) program of 16 sub-millimetre faint ($S_{B6} = 0.1 - 0.99$ mJy) ALMA sources from the ALMA Spectroscopic Survey in the Hubble Ultra Deep Field (ASPECS; Walter et al. 2016) survey. They identify nominal metallicities and electron densities suggesting the galaxies follow the same scaling relations as typical star-forming galaxies at the same epoch. However, besides from a relatively small number of sources, the sample does not include the most dust-obscured, bright (>1 mJy), sub-millimetre sources, and therefore the nature of these extreme sources remains unclear.

To this end, in this paper, we present an analysis of the rest-frame optical spectroscopic properties of every known ($>3\sigma$) ALMA detected sources currently observed with NIRSpec/MSA. In Section 2 we define the initial sample of ALMA – NIRSpec galaxies that we use in our analysis whilst in Section 3 we present the observations, data reduction and analysis undertaken on these sources, before constructing a robust final sample. In Section 4 we give our results and discuss their implications before summarising our main conclusions in Section 5. Throughout the paper, we assume a Λ CDM cosmology with $\Omega_m = 0.3$, $\Omega_\Lambda = 0.7$, and $H_0 = 70$ km s $^{-1}$ Mpc $^{-1}$. All quoted magnitudes are on the AB system (Oke & Gunn 1983), and stellar masses are calculated assuming a Kroupa initial mass function (IMF) (Kroupa 2002). All uncertainties on median values are derived from bootstrapped resampling.

2. Sample Selection

To constrain the ionised interstellar medium properties (e.g. metallicity, electron density, ionisation parameter) of known ALMA sources, we require at least median resolution ($R \gtrsim 1000$) spectroscopy that samples the rest-frame optical to near-infrared wavelength regime. This provides both the spectral coverage for key emission line features (e.g. $H\alpha$, $H\beta$, [OIII]) as well as the resolution (≤ 127 km s $^{-1}$) to resolve line complexes such as [NII]/ $H\alpha$.

Thus, to build a sample of galaxies with both median resolution spectroscopy and prior far-infrared detections, we use observations from the DeepDive Survey (PID #3567, PI: Valentino). For full details of the DeepDive Survey see Ito et al. (2025). In brief, DeepDive is a JWST Cycle-2 program using the NIRSpec Mirco-Shutter Array (MSA; Jakobsen et al. 2022), targeting quiescent galaxies at $z \approx 3-4$ with the median resolution G235M/F170LP filter grating pair. In addition to the primary targets, additional filler targets of known far-infrared detected sources were also included in the MSA masks, in total giving spectra for 555 galaxies across a broad range of redshift (see Ito et al. (2025) for details).

We utilise this sample from DeepDive, in addition to the full DAWN JWST Archive (DJA¹; Valentino et al. 2023; Heintz et al. 2025) v4.4 that contains all public NIRSpec spectra to date. Next, we compile a list of known ALMA detected sources. Specifically, we utilise the ECOlogy for Galaxies using ALMA archive and Legacy surveys (ECOGAL; Lee et al. 2025) database in the UKIDSS Ultra-DEEP Survey (UDS; Lawrence

¹ <https://doi.org/10.5281/zenodo.15472354>

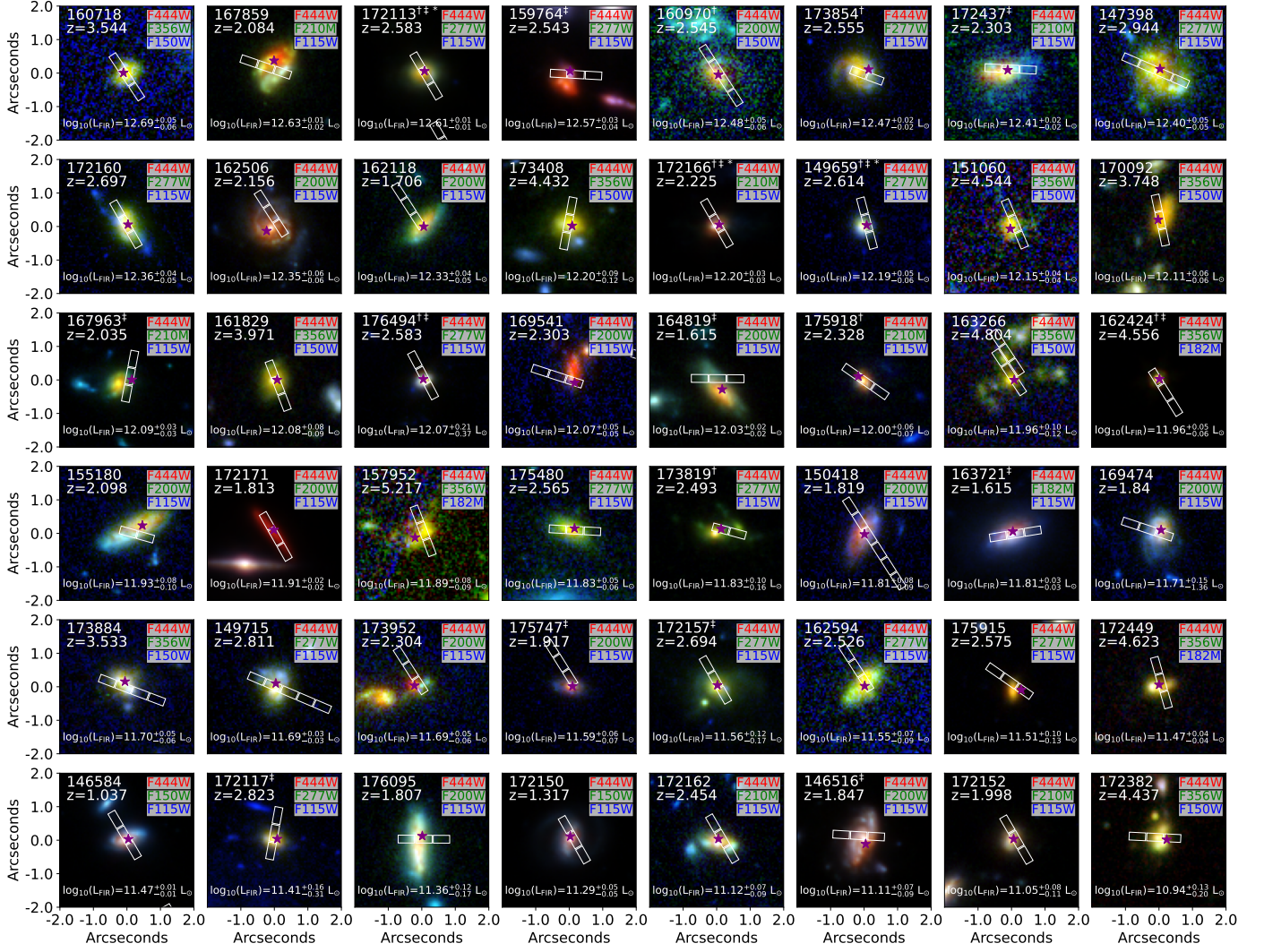


Fig. 1: JWST/NIRCam false colour images for the final sample of 48 ALMA – NIRSpect galaxies ranked in descending far-infrared luminosity (L_{FIR}). For each source we show the $4'' \times 4''$ cutout as labelled with the DJA-ID, spectroscopic redshift, far-infrared luminosity, ALMA peak flux centroid (purple star) and NIRSpect MSA slits (white boxes) for one dither position. For each source we select the NIRCam filter that corresponds to rest-frame $2\mu\text{m}$ (R, near-infrared), $0.7\mu\text{m}$ (G, optical) and $0.3\mu\text{m}$ (B, ultra-violet). Sources identified as AGN (see Sec. 4.2) are highlighted, where † indicates broad emission lines, ‡ indicates an X-ray counterpart and * highlights elevated optical-line ratios.

et al. 2007) extragalactic field, in addition to A3COSMOS² (Liu et al. 2019) and A3GOODS-S² (Adscheid et al. 2024) in the Cosmic Evolution Survey (COSMOS; Scoville et al. 2007) and Great Observatories Origins Deep Survey – South (GOODS-S; Giavalisco et al. 2004) extragalactic fields respectively. The ECOGAL database provides a list of ALMA detected sources in regions that overlap with the HST Cosmic Assembly Near-infrared Deep Extragalactic Legacy Survey (CANDELS; Grogin et al. 2011) footprint (see Lee et al. 2025 for details), whilst A3COSMOS and A3GOODS-S present all sources detected in the ALMA archive in their respective fields. We further make use of a list of previously characterised bright ($S_{870\mu\text{m}} > 1 \text{ mJy}$) sub-millimetre galaxies in the literature with high-resolution ($< 0''.6$) counterparts, as presented in Gillman et al. (2023), which includes ALMA-detected SCUBA-2 sources from Dudzevičiūtė et al. 2020.

² v20250312 <https://uni-bonn.sciebo.de/s/0LrfuA1s2YP3cz?path=%2F>

Using this combined list, we cross match the position of the NIRSpect slit to ALMA source positions with a search radius of $r = 0''.5$. In doing so, we both capture any NIRSpect source with a far-infrared ALMA detection, as well as known sub-millimetre bright galaxies that fall outside the HST-CANDELS footprint. In total we identify 153 unique galaxies with NIRSpect spectra, of which 32 have PRISM spectra and 121 have median resolution (or higher) grating spectra.

3. Data Reduction and Analysis

Having defined an initial sample of 121 ALMA sources with median, or higher, resolution NIRSpect observations, we now first analyse their photometric properties, at both near and far-infrared wavelengths, in addition to their spectroscopic properties, to establish the presence of key rest-frame optical emission lines required to reveal their interstellar medium properties, before defining a robust final sample.

3.1. UV-NIR Photometry and SED Fitting

We use the public database of existing imaging in well studied extragalactic fields from DJA (for details see [Valentino et al. 2023](#)) that incorporates deep multi-band HST (ACS + WFC3) observations from the HST-CANDELS program and JWST (NIRCam + MIRI) observational programs such as; The Public Release IMaging for Extragalactic Research (PRIMER; [Dunlop et al. 2021](#)), JADES Survey ([Eisenstein et al. 2023](#)). For full details of the observational imaging programs we refer the reader to DJA³. Nearly 78% (94/121) of the sources fall within the either UDS field (50 sources) or GOODS-S (44 sources) whilst the remaining 27 sources come from the COSMOS field extragalactic field. Figure 1 shows the NIRCam false colour images for the final sample as defined in Section 3.5.

For each source we adopt the photometry from DJA. As detailed in ([Valentino et al. 2023](#)), we measure the photometry using the pythonic version of the Source Extractor code `sep v1.2.1` ([Bertin & Arnouts 1996](#); [Barbary et al. 2016](#)). We use a combined NIRCam long-wavelength (LW) image as a detection image and measure the flux in circular apertures with a diameter of 0.5 and corrected to "total" values with Kron apertures ([Kron 1980](#)) which were computed on the LW combined detection image. To derive the stellar mass of the sources, we model their SEDs using the Bayesian Analysis of Galaxies for Physical Inference and Parameter Estimation (`bagpipes`; [Carnall et al. 2018](#)) code, with a double power-law star formation history and a [Calzetti et al. \(2000\)](#) dust attenuation law. We adopt the [Bruzual & Charlot \(2003\)](#) stellar population models with a [Kroupa \(2002\)](#) initial mass function. We adopt uniform priors for the stellar mass and A_V with a logarithmic prior on the metallicity (see [Ito et al. 2025](#) for full details). Finally, we fixed the redshift to the spectroscopic redshift as estimated from `msaexp` (see Sec. 3.4). The SED properties of the final sample (Section 3.5) is presented in Appendix C.

3.2. MIR-Radio Photometry and SED Fitting

In addition to the ALMA observations from which our sample was defined (see Table A), we compile the mid-to far-infrared photometry for our sources from the literature. For sources in the UDS field we adopt the Herschel de-blended photometry catalogue as utilised in ([Swinbank et al. 2014](#); [Dudzevičiūtė et al. 2020](#)), as well as the ALMA photometry from ECOGAL ([Lee et al. 2025](#)). For COSMOS, we use an updated super-deblended catalogue from [Jin et al. \(2018\)](#), whilst for GOODS-S we adopt the infrared photometry from [Magnelli et al. \(2014\)](#). We identify the photometry for each source by cross matching the photometry catalogues with the NIRSpec source position (see Table A), finding all matches within 1". We enforce a detection criteria of 3σ in a given band, defining 3σ upper limits for all fluxes detected at a lower significance. We remove any photometry that samples rest-frame blueward of $40\mu\text{m}$ as this requires multi-temperature blackbody models that can incorporate the warm dust emission of the sources (e.g. [Draine et al. 2007](#); [da Cunha et al. 2008](#)), which is beyond the scope of this paper.

To derive the far-infrared SED properties of the sources we utilise the Multimodal Estimation Routine for the Cosmological Unravelling of Rest-frame Infrared Uniformised Spectra (`mercurius`; [Witstok et al. 2022](#)) code, which performs a Bayesian least-squares fitting of a modified blackbody fitting to far-infrared SED, examples of which are shown in Figure

2. Given the well known degeneracy between dust temperature (T_d) and far-infrared slope (β), we fix the far-infrared slope to $\beta=1.8$, consistent with values derived for DSFGs from Herschel and ALMA observations (e.g. [Magnelli et al. 2014](#); [Cunha et al. 2015](#); [Ward et al. 2024a](#); [Bing et al. 2024](#)). For each source we fixed the redshift to the spectroscopic redshift as estimated from `msaexp` (see Sec. 3.4). We further assume optically thin dust and adopt a flat prior on the dust mass in the range $\log_{10}(M_d[M_\odot])=4.0-12.0$. For the dust temperature, we used the default gamma distribution, shifted to the temperature of the cosmic microwave background, with shape parameter fixed to 1.5, with a maximum dust temperature of 150 K. For 25 sources with a single far-infrared detection (excluding limits), we further fix the dust temperature to $T_d=30$ K. We adopt the built-in dust emissivity coefficient $\kappa=\kappa_0(\nu/\nu_0)^\beta$ with $\kappa_0=8.94\text{ cm}^2\text{ g}^{-1}$ at $\nu_0=1900\text{ GHz}$ ($\sim 158\mu\text{m}$ [Hirashita et al. 2014](#)). Details of the mercurius blackbody fits, including MCMC corner plots, for the final sample (Sec. 3.5), are given in Section 6, whilst the derived physical parameters are given in Appendix C.

3.3. Rest-Frame Optical Morphology

To constrain the rest-frame optical morphology of the ALMA detected galaxies we use `PySersic` ([Pasha & Miller 2023](#)). `PySersic` is a python-based Bayesian inference code which fits parametric (Sérsic) models to galaxy light distributions. For each galaxy, we fit the Sérsic profiles to the available JWST NIRCam wide-band imaging in 4.8×4.8 size cutouts, using point spread functions PSFs derived from `PSFEx` ([Bertin 2011](#)) using the same procedure as [Genin et al. \(2025\)](#). Nearby sources are detected down to a 1.5σ level and masked using the segmentation map in the fitting process. We then derive the rest-frame optical ($0.5\mu\text{m}$) size by selecting the NIRCam long-wavelength filter with rest-frame wavelength closest to $0.5\mu\text{m}$ in a similar methodology to [Gillman et al. \(2023\)](#). The derived sizes and Sérsic indices, for the final sample (see Sec. 3.5), are given in Appendix C.

3.4. Spectroscopy

To constrain the ionised interstellar medium properties of the far-infrared detected NIRSpec sources, we first measure the continuum level in the spectra before flux calibrating and quantifying the emission-line properties.

3.4.1. Continuum and Flux Calibration

To model the continuum we run `msaexp` ([Brammer 2023](#); [de Graaff et al. 2025](#)). Using a non-parametric approach, with a combination of splines and Gaussian models for the emission lines, `msaexp` produces a robust estimate of the continuum level, in addition to the noise spectrum, as a function of wavelength. For our analysis we use 13 knot-splines to model the continuum. The `msaexp` pipeline further extends the standard wavelength coverage of the NIRSpec spectra, to the full red extension using a combination of long-pass filter and the projection on the detector (see [Valentino et al. 2025](#) for details).

As described in [Ito et al. \(2025\)](#), we utilise the available multi-wavelength photometry to flux calibrate the spectra. We model any potential flux losses using a polynomial function,

³ <https://dawn-cph.github.io/dja/imaging/v7/>

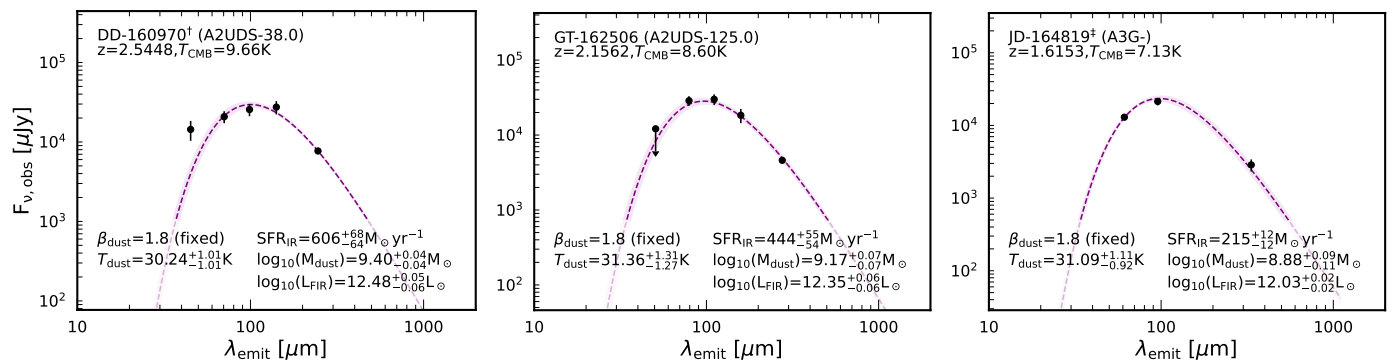


Fig. 2: Three examples of the mercurius far-infrared modified blackbody modelling. For each source show the photometry (black points; upper limits shown as arrows) and best-fit blackbody curve (purple-dashed line) and 1σ uncertainty (purple shaded region). We report the best-fit parameter in each panel, as well as NIRSpect (and ALMA) source ID, redshift and CMB temperature. Sources identified as AGN (see Sec. 4.2) are highlighted, where † indicates broad emission lines, ‡ indicates an X-ray counterpart and * highlights elevated optical-line ratios. The SEDs, and MCMC corner plots, of the full sample are given in Section 6.

whose order reflects the number of available photometric bands.⁴ We further apply a wavelength-dependent correction that accounts for parts of the spectrum beyond the nominal cut-off (see Ito et al. 2025 for full details.). Furthermore, *msaexp* defines the spectroscopic redshift of the source through the detection of multiple emission lines. We show examples of the rest-frame, continuum subtracted, spectra in Figure 3, with the spectra for the final sample (Sec. 3.5) shown in Appendix D.

3.4.2. Emission-Line Fitting

Next, we perform the emission-line fitting to the continuum subtracted spectrum using the *mpfit*⁵ python code that employs the Levenberg-Marquardt technique to solve the least-squares problem. We use *mpfit* instead of *msaexp* as it allows more flexibility in the modelling of multiple Gaussian profiles with interconnected properties. For instance to model line complexes such as $H\alpha$ -[NII]-[SII] or [OIII]-H β , we use multiple Gaussian profiles with consistent redshifts and emission-line widths, whilst the amplitude of each emission line is free to vary. For single emission-line features we fit a single Gaussian model with emission-line width, amplitude and redshift free to vary. For all emission-lines the minimum width is fixed by the instrumental broadening of the NIRSpect MSA instrument as a function of wavelength. We adopt the post-flight improved resolution of NIRSpect, as estimated by recent studies to be of order $\sim 30\%$ higher resolving power (e.g. Slob et al. 2024; Shajib et al. 2025), which results in velocity resolution of $\leq 100 \text{ km s}^{-1}$ for median-resolution spectroscopy at the wavelength of $H\alpha$. We define any emission-line with signal-to-noise (S/N) greater than three as detected, placing 3σ limits derived from the *msaexp* noise spectrum, on non-detections.

To understand whether the emission-line properties are originating from star-forming regions of the galaxy or in fact driven by Type-1 Active Galactic Nuclei (AGN) activity, we further fit each emission line feature as a double Gaussian with a narrow and broad component. We constrain the fitting such that the FWHM of the narrow component is less than 800 km/s and

has independent line ratios whilst having consistent redshift. To evaluate the presence of the broad component we calculate the reduced chi-squared (χ_{red}^2) and Bayesian Information Criteria (BIC) of each model, defined as,

$$\chi^2 = \sum_i^{N_d} r_i^2 \quad (1)$$

$$\chi_{\text{red.}}^2 = \chi^2 / (N_d - N_{\text{varys}}) \quad (2)$$

$$\text{BIC} = \chi^2 + N_{\text{varys}} \times \ln(N_d) \quad (3)$$

where $\sum_i^{N_d} r_i^2$ is the sum of the residual spectrum, N_d is the number of data points, and N_{varys} is the number of variable parameters. Both of these statistical parameters reflect the goodness of fit whilst the BIC parameter penalises models with a large number of parameters and is commonly used to determine between two parametric models (e.g. Head et al. 2014; Lange et al. 2016). The model with the lower BIC values and $\chi_{\text{red.}}^2$ close to unity is preferred.

3.5. Final Sample

Having constrained the photometric and spectroscopic properties of the 121 ALMA sources detected with NIRSpect grating spectra, we now define a final sample with robust properties. First we remove 14 sources for which *msaexp* can not determine the spectroscopic redshift, due to low signal to noise and or lack of emission lines. Next, we remove 52 sources where, given the spectroscopic redshift of the source, the rest-frame wavelength of the NIRSpect spectra does not encapsulate the [NII]/ $H\alpha$ complex, which is crucial to measure the gas-phase metallicity, or for which $H\alpha$ is not detected ($S/N < 3$). We ensure all sources have a well sampled observed-frame optical to near-infrared ($0.4 - 1.6 \mu\text{m}$) with a minimum of four filters and we thus remove three sources that do not have JWST (NIRCam or MIRI) imaging. Similarly, in the far-infrared we remove four sources whose ALMA detection is less than 3σ .

This results in a final sample of 48 sources with $> 3\sigma$ ALMA continuum and $H\alpha$ detections, as presented in Table A. The final sample has a median spectroscopic redshift of $z = 2.535 \pm 0.100$ with a 16th – 84th percentile range of $z = 1.830 - 3.855$. We further derive a median stellar mass $\log_{10}(M_* [M_\odot]) = 10.8 \pm 0.1$ with a

⁴ We note that given the stochastic placement of MSA slits, driven by the archival nature of our sample, the spectral properties may not always represent the full galaxy integrated properties.

⁵ <https://millenia.cars.aps.anl.gov/software/python/mpfit.html>

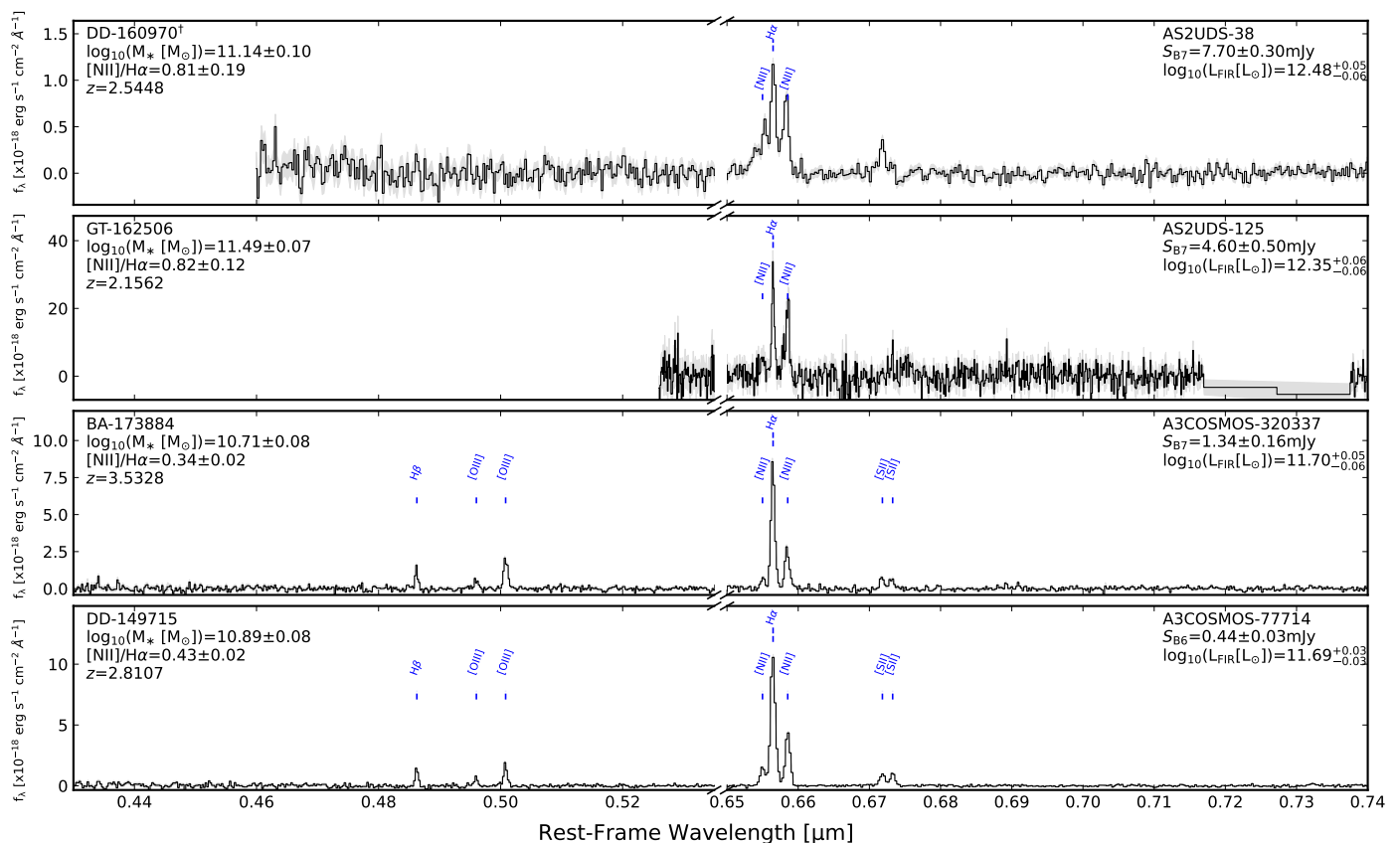


Fig. 3: JWST/NIRSspec spectra for four galaxies in the sample across a range of far-infrared luminosity. For each source we show the NIRSspec spectra (and 1σ uncertainty) from rest-frame $0.36\text{--}0.54\mu\text{m}$ highlighting the $[\text{OIII}]/\text{H}\beta$ complex and $0.65\text{--}0.74\mu\text{m}$ highlighting the $[\text{NII}]/\text{H}\alpha$ complex, with detected ($>3\sigma$) emission lines labelled. We further indicate the NIRSspec-ID, bagpipes derived stellar mass, observed $[\text{NII}]/\text{H}\alpha$ ratio, spectroscopic redshift as well as ALMA-ID, ALMA flux density and far-infrared luminosity of each source. Sources identified as AGN (see Sec. 4.2) are highlighted, where † indicates broad emission lines, ‡ indicates an X-ray counterpart and * highlights elevated optical-line ratios.

16–84th percentile range of $\log_{10}(M_* [M_\odot]) = 10.5\text{--}11.2$, whilst from the *mercurius* modelling we establish a median dust mass of $\log_{10}(M_d [M_\odot]) = 8.7 \pm 0.1$ with a 16–84th percentile range of $\log_{10}(M_d [M_\odot]) = 8.1\text{--}9.1$. A summary of the SED derived properties for the final sample is given in Appendix C. Having established a robust sample of 48 ALMA sources with well-defined photometric and spectroscopic properties we now investigate their ionised interstellar medium properties in the context of the broader galaxy population at a similar epoch.

4. Results and Discussion

Due to the inhomogeneous nature of the far-infrared selection, our final sample of ALMA sources covers a broad range sub-millimetre flux density. As detailed in Table A, 22 sources (46%) are detected in ALMA Band 7, of which 9 are part of the ALMA SCUBA-2 UDS survey (AS2UDS; Stach et al. 2019; Dudzevičiūtė et al. 2020) and represent sub-millimetre bright (>1 mJy) galaxies (SMGs) with $850\mu\text{m}$ flux densities ranging from $S_{B7} = 1.02\text{--}7.70$ mJy which is comparable to the full AS2UDS sample (e.g. Dudzevičiūtė et al. 2020) and the broader SMG population at this epoch (e.g. Hodge et al. 2013; Casey et al. 2014; Simpson et al. 2020). The rest of the sample is made up of ALMA Band 6 (35%), Band 4 (15%), Band 8 (2%) and Band 9 (2%) with a median ALMA signal to

noise of $S/N = 5.72 \pm 0.47$ and a 16th–84th percentile range of $S/N = 3.53\text{--}9.27$.

To homogenise the sample, we utilise the far-infrared luminosity (L_{FIR}), as derived from blackbody fitting (see Sec 3.2). We note the L_{FIR} as derived from *mercurius* corresponds to the integrated blackbody emission and does not include warm or mid-infrared dust components. Typically the infrared luminosity ($8\mu\text{m}\text{--}1000\mu\text{m}$) is a factor of $\approx 1.6\times$ (~ 0.2 dex) higher than the far-infrared luminosity ($40\mu\text{m}\text{--}1000\mu\text{m}$) (e.g. Rémy-Ruyer et al. 2015; Dudzevičiūtė et al. 2020). The ALMA–NIRSspec sample has a median far-infrared luminosity of $\log_{10}(L_{\text{FIR}} [L_\odot]) = 11.95 \pm 0.08$ with a 16th–84th percentile range of $\log_{10}(L_{\text{FIR}} [L_\odot]) = 11.47\text{--}12.38$.

By construction, the sample encapsulates a full range of far-infrared luminosities from far-infrared bright systems comparable to those from AS2UDS with a median value of $\log_{10}(L_{\text{IR}} [L_\odot]) = 12.45 \pm 0.02$ (Dudzevičiūtė et al. 2020; Gillman et al. 2024) or the ALMA LABOCA ECDFS Submillimeter Survey (ALESS; Hodge et al. 2013; Swinbank et al. 2014) sample with a median value of $\log_{10}(L_{\text{IR}} [L_\odot]) = 12.47 \pm 0.04$ at a median redshift of $z = 2.5 \pm 0.2$. The sample also includes nine lower luminosity ($\log_{10}(L_{\text{FIR}} [L_\odot]) < 11.5$) sources, in the regime of luminous infrared galaxies (LIRGS; Sanders et al. 1988) comparable to studies of fainter DSFGs (e.g. Elbaz et al. 2011; Aravena et al. 2016; Suzuki et al. 2021; McKay et al. 2025; Kiyota et al. 2026).

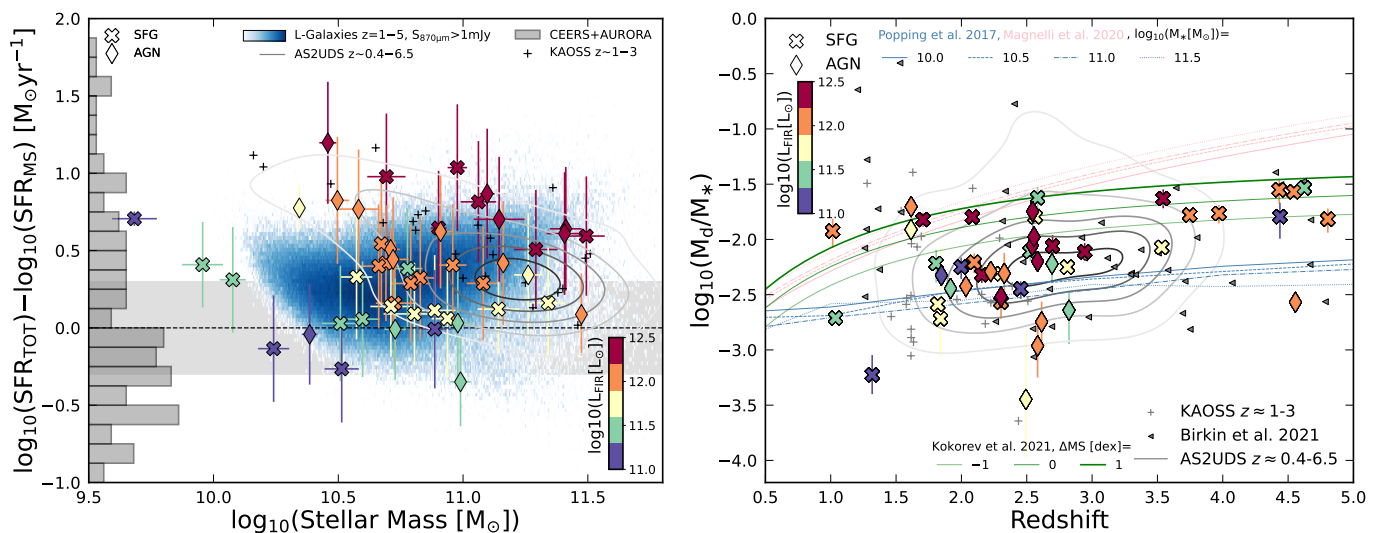


Fig. 4: Left: The offset to the star-forming main sequence relation from Poppo et al. (2023) as function of stellar mass. The ALMA-NIRSpec galaxies are coloured by their far-infrared luminosity (L_{FIR}) and we indicate the intrinsic 0.3 dex scatter in the main-sequence (grey shaded region). We include comparison samples of high-redshift star-forming galaxies from the CEERS and AURORA surveys (grey histogram), as well as $\text{H}\alpha$ -detected SMGs from the KAOSS survey (Birkin 2022; Birkin et al. 2024b) (grey pluses) and AS2UDS survey (Dudzevičiūtė et al. 2020) (grey contours), in addition to far-infrared bright ($S_{870\mu\text{m}} > 1\text{mJy}$) galaxies at $z = 1 - 5$ (blue density region) from the L-Galaxies SAM (Araya-Araya et al. 2025a). The ALMA-NIRSpec sample shows a strong correlation between main sequence offset and far-infrared luminosity, with far-infrared bright ($\log_{10}(L_{\text{FIR}}[\text{L}_{\odot}]) > 12.0$) galaxies falling (≥ 0.5 dex) above the main-sequence relation, consistent with other bright far-infrared detected, and simulated, galaxies at the same epoch. **Right:** The dust to stellar mass ratio as a function of redshift with the ALMA-NIRSpec galaxies coloured by far-infrared luminosity. We again include comparison samples of high-redshift SMGs from KAOSS, AS2UDS as well as CO-selected SMGs from Birkin et al. (2021). Our sample has similar dust to stellar mass ratios when compared to traditional SMG samples at the same redshift. We also show the observational scaling relation from Magnelli et al. (2020) (pink lines) and the Santa-Cruz SAM (blue lines) (Popping et al. 2017) for a range of stellar masses, in addition to the observationally-derived scaling from Kokorev et al. (2021) at fixed stellar mass ($\log_{10}(M_{*}[\text{M}_{\odot}]) = 10.8$) as a function of main sequence offset (green lines).

In Figure 1 we show the NIRCcam false colour images for the 48 ALMA-NIRSpec galaxies, centred on the NIRCcam F444W detected source, ranked in descending far-infrared luminosity. For each source we select the NIRCcam filters that sample the rest-frame $2\mu\text{m}$ (R), $0.7\mu\text{m}$ (G) and $0.3\mu\text{m}$ (B). We further indicate the NIRSpec-ID, spectroscopic redshift, far-infrared luminosity and ALMA source position. From Figure 1 it is clear the sample represents a broad range of optical to near-infrared morphologies from isolated discs and compact point sources (e.g. ID:175747, ID:175918) to extended, potentially interacting sources (e.g. ID:173952, ID:172382). There is no clear morphological correlation with far-infrared luminosity, with both high luminosity ($\log_{10}(L_{\text{IR}}[\text{L}_{\odot}]) > 12.0$) and lower luminosity ($\log_{10}(L_{\text{IR}}[\text{L}_{\odot}]) < 11.5$) galaxies, exhibiting a range of rest-frame UV/optical/infrared colours and morphologies. This is also in agreement with recent morphological studies of far-infrared detected galaxies (e.g. Gillman et al. 2024; Polletta et al. 2024; Chan et al. 2025).

In terms of rest-frame optical morphology the sample has a median $0.5\mu\text{m}$ size of $R_{e,0.5\mu\text{m}} = 2.74 \pm 0.33$ kpc. Adopting rest-frame optical mass size relation from Ward et al. (2024b) which is derived for star-forming galaxies in the CEERS survey, we establish on average the ALMA sources fall slightly below the relation with $\Delta R_{e,0.5\mu\text{m}}[\text{dex}] = \log_{10}(R_{e,0.5\mu\text{m},\text{PySersic}}) - \log_{10}(R_{e,0.5\mu\text{m},\text{Ward}}) = -0.08 \pm 0.03$, although we note the Ward et al. (2024b) relation is defined at lower ($< 10^{10.5}\text{M}_{\odot}$) stellar masses. Splitting the sample into far-infrared bright sources ($\log_{10}(L_{\text{IR}}[\text{L}_{\odot}]) > 12.0$) and far-infrared faint sources

($\log_{10}(L_{\text{IR}}[\text{L}_{\odot}]) < 11.5$), we establish no difference in optical sizes at fixed stellar mass, with $\Delta R_{e,0.5\mu\text{m}}[\text{dex}] = -0.11 \pm 0.03$ and $\Delta R_{e,0.5\mu\text{m}}[\text{dex}] = -0.11 \pm 0.06$, respectively. This is consistent with recent studies of far-infrared detected galaxies with JWST, which suggest DSFGs follow the same stellar mass size relation as less dust obscured sources (e.g. Boogaard et al. 2023; Gillman et al. 2024; McKinney et al. 2024; Ren et al. 2024).

4.1. Star-Formation and Dust Content

In Figure 4a, we show the position of the ALMA-NIRSpec galaxies in relation to the star-forming main-sequence at their epoch as defined from Poppo et al. (2023)⁶. For each galaxy we define the total star-formation rate (SFR_{tot}) as the observed (not dust corrected) $\text{H}\alpha$ star-formation rate ($\text{SFR}_{\text{H}\alpha}$)⁷ plus SFR_{FIR} as derived in Sec. 3.2. We further colour the ALMA-NIRSpec galaxies by their far-infrared luminosity, identifying a clear trend, of galaxies above $\log_{10}(M_{*}[\text{M}_{\odot}]) > 10.5$ with $\log_{10}(L_{\text{FIR}}[\text{L}_{\odot}]) < 11.5$ falling on or below the main sequence, whilst those at $\log_{10}(L_{\text{FIR}}[\text{L}_{\odot}]) > 11.5$ lie above the main sequence at their stellar mass.

For comparison, we include sources from recent JWST NIRSpec surveys of typical star-forming galaxies where there is no (detectable) far-infrared star formation contribution. In partic-

⁶ We note the exact offset depends on the functional form of the main sequence, where a linear power-law (e.g. Pearson et al. 2018) would result in a smaller offset at the highest masses

⁷ We note here we are assuming all $\text{H}\alpha$ narrow flux is due to star formation activity, so in this respect is an upper limit.

ular we utilise results from the Assembly of Ultradeep Rest-optical Observations Revealing Astrophysics (AURORA) survey (Shapley et al. 2025) and the Cosmic Evolution Early Release Science (CEERS) Survey (Shapley et al. 2023). From these surveys we selected a redshift matched sample of 112 (57 AURORA, 55 CEERS) star-forming galaxies that have no indication of broad-line AGN activity⁸ and emission-lines fluxes at $S/N > 3$. This subsample of CEERS+AURORA galaxies, as indicated by the grey histogram in Figure 4a, has a median stellar mass of $\log_{10}(M_*M_\odot) = 9.5 \pm 0.1$ and a median SED derived star formation rate of $SFR = 6 \pm 2 M_\odot \text{ yr}^{-1}$.

We further include literature samples of SMGs from the AS2UDS survey (Dudzevičiūtė et al. 2020) and the KMOS-ALMA Observations of Submillimetre Sources (KAOSS; Birkin 2022; Birkin et al. 2024b; Taylor et al. prep). For the KAOSS sources we use the same SFR_{tot} definition as for the ALMA-NIRSpec sample (uncorrected $H\alpha$ star-formation rate plus far-infrared star-formation) as derived in Birkin (2022). We scale the magphys derived total star-formation rates of the AS2UDS sample by a factor of $\approx 1.3\times$ which accounts for the scaling between SFR_{tot} , as defined above, and SFR_{magphys} (see Dudzevičiūtė et al. (2020); Birkin (2022) for details). In addition to the observational studies, we make use of recent results from L-Galaxies semi-analytic model (Araya-Araya et al. 2025a,b) that is re-calibrated using an Markov chain Monte Carlo (MCMC) approach, to provide an improved match to observationally-inferred number densities of both SMGs and massive quiescent galaxies populations. We select a sub-sample of far-infrared bright ($S_{870\mu\text{m}} > 1\text{mJy}$) at $z = 1-5$ galaxies, whose stellar mass and star-formation properties reflect the full far-infrared bright population in L-Galaxies. We calculate the main-sequence offset of the L-Galaxies sample using the instantaneous star-formation rate within the snapshot, which is equates to a 5.6 Myr timescale at $z = 1$ and increases to 18.19 Myr at $z = 5$ ⁹.

On average the ALMA-NIRSpec galaxies fall 0.32 ± 0.07 dex above the main sequence, with the highest infrared luminosity sources lying well above the main sequence (≥ 0.5 dex), with a similar main sequence offset to the AS2UDS and KAOSS samples at the same stellar mass. In contrast, the CEERS+AURORA sample (as indicated by the grey histogram in Figure 4a), of less-massive, less dust-obscured galaxies, scatter about the main-sequence with a median main sequence offset of -0.11 ± 0.07 dex, which is within the intrinsic ≈ 0.3 dex intrinsic scatter of the main sequence relation (e.g. Popesso et al. 2023). The L-Galaxies sources, with a $16^{\text{th}}-84^{\text{th}}$ stellar mass range of $\log_{10}(M_*M_\odot) = 10.50-11.0$, have a median main sequence offset of 0.28 dex, which is just within the 0.3 dex intrinsic scatter of the main-sequence, but predominately at higher specific star-formation rates compared to typical star-forming galaxies from CEERS and AURORA at the same epoch. For L-Galaxies sources above $\log_{10}(M_*[M_\odot]) = 11.0$, we identify an increased main sequence offset of 0.43 dex, in a similar trend to the ALMA-NIRSpec galaxies.

In Figure 4b, we show the dust to stellar mass ratio of the ALMA-NIRSpec galaxies as a function of redshift, coloured by their far-infrared luminosity. We again include the samples of SMGs from AS2UDS and KAOSS, as well as CO-selected SMGs from Birkin et al. (2021). We rescale the dust masses

of the AS2UDS and KAOSS samples, derived from magphys, by a factor 1.2 (as derived in Dudzevičiūtė et al. 2020), to account for the differences between modified blackbody and full multi-wavelength SED derived dust masses (see also Hunt et al. 2019). The ALMA-NIRSpec galaxies have median dust fraction of $\log_{10}(M_d/M_*) = -2.20 \pm 0.08$ with a $16^{\text{th}}-84^{\text{th}}$ range of $\log_{10}(M_d/M_*) = -2.58$ to -1.78 . On average the sample is consistent with the sub-millimetre bright comparison samples at a median redshift of $z = 2.5$, but exhibits higher dust fractions at higher redshift, with the ALMA-NIRSpec galaxies at $z > 3$ having a median dust fraction of $\log_{10}(M_d/M_*) = -1.78 \pm 0.09$.

In Figure 4b we include predictions from the fiducial model of the Santa-Cruz SAM Popping et al. (2014, 2017), which tracks the lifecycle of dust with prescriptions for dust production, growth and destruction. We show the models predicted evolution of the dust fraction as a function of redshift (blue lines) for fixed stellar masses ($\log_{10}(M_*[M_\odot]) = 10.0, 10.5, 11.0, 11.5$). We also show the observationally-derived scaling relation from Magnelli et al. (2020), for the same stellar mass ranges (pink lines), as well as the relation from Kokorev et al. (2021), at the median stellar mass of the ALMA-NIRSpec sample ($\log_{10}(M_*[M_\odot]) = 10.8$), as a function of main sequence offset (green lines), at $-1, 0$ and 1 dex off the main sequence. At the median redshift of the sample ($z = 2.5$), the ALMA-NIRSpec sample is more aligned with the Popping et al. (2017) model, whose dust growth its implicitly tied to the metal budget of the galaxies, which is systematically lower than the dust fractions derived from far-infrared observations of main-sequence galaxies in Magnelli et al. (2020); Kokorev et al. (2021). At higher redshift ($z > 3$) the ALMA-NIRSpec sample, shows higher dust fractions, and is more aligned with the observationally derived Magnelli et al. (2020); Kokorev et al. (2021) relations.

Figures 1 & 4 demonstrate that despite the inhomogeneous selection of our sample, on average the ALMA-NIRSpec galaxies reflect the broader population of uniformly selected (e.g. $870\mu\text{m}$ selected) DSFGs at their epoch, both in terms of morphology, and photometric properties (e.g. stellar mass, star formation rate and, dust mass). We now focus on analysing the properties of their ionised interstellar medium, as unprecedentedly revealed by the NIRSpec grating spectra.

4.2. Ionisation Origin

Prior to analysing the properties of the ionised interstellar medium of the ALMA-NIRSpec, we first investigate whether their emission is the result of AGN activity or star-formation.

First, we check for the X-ray counterparts to the ALMA-NIRSpec galaxies, requiring any source with an X-ray detection to be greater 10^{42} erg/s to be flagged as an AGN. We adopt this threshold given that fainter X-ray emission can have stellar origins (e.g. X-ray binaries, shocks) and thus does not necessarily indicate the presence of AGN activity (e.g. Lehmer et al. 2010; Hickox & Alexander 2018).

For sources in the UDS field we adopt the 600ks Chandra Legacy Survey of UDS as presented in Kocevski et al. (2018), whilst for GOODS-S and COSMOS we adopt the 7Ms Chandra Deep Field-South survey as presented in Luo et al. (2017) and the 4.6Ms Chandra COSMOS-Legacy survey from Civano et al. (2016) respectively. We crossmatch our NIRSpec source positions to within $1''$ of the X-ray sources, which accounts for both the resolution and astrometry offsets between Chandra and JWST (e.g. Lyu et al. 2022; Gillman et al. 2025). We identify 15 counterparts (31% of the sample) within $0''.8$, all with an absorption corrected X-ray luminosity $> 10^{42}$ erg/s with a median value

⁸ $\text{agnflag}=0$, see Shapley et al. (2023, 2025) for details

⁹ We note this is not exactly the same as the observational total star formation rate. The results of our analysis are unchanged if we adopt the snapshot average star formation rate from the simulation, which varies from 112 Myr timescale at $z = 1$ to 368 Myr at $z = 5$.

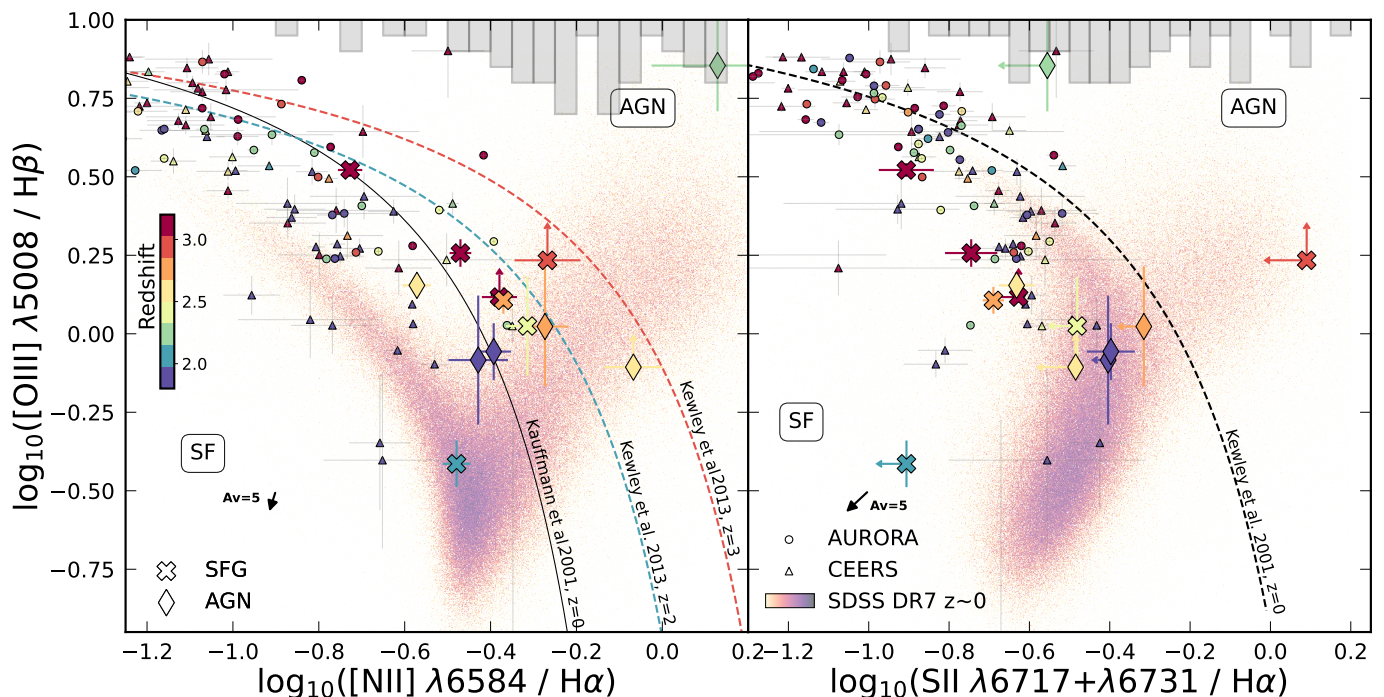


Fig. 5: Observed (dust-uncorrected) $[O\text{III}]\lambda 5008 / H\beta$ as function of $[N\text{II}]/H\alpha$ (left) and $[S\text{II}]/H\alpha$ (right). Sources with $S/N < 3$ in the respective emission-line are shown as limits. The distribution of $[N\text{II}]/H\alpha$ and $[S\text{II}]/H\alpha$ for the full sample is shown by the grey histograms. We show comparison samples of typical star-forming galaxies at $z \sim 0$ (red density) from the Sloan Digital Sky Survey (SDSS; Brinchmann et al. 2004), as well as a redshift matched sample of star-forming galaxies from the CEERS (Shapley et al. 2023) and AURORA Surveys Shapley et al. (2025). The black solid curve shows the division between star-formation activity and AGN (Kauffmann et al. 2003) at $z = 0$ whilst the theoretical demarcation at $z = 2$ and $z = 3$ from (Kewley et al. 2013) is given by the blue- and red-dashed lines respectively. The black arrow indicates the impact of $A_V = 5$ dust correction using a Calzetti et al. (2000) dust law. The majority of ALMA – NIRSpec galaxies are consistent with typical SFGs at the same epoch, pushing to lower $[O\text{III}]/H\beta$ line ratios, with only three galaxies showing AGN-like optical line diagnostics.

of $\log_{10}(L_{Xc}[\text{erg/s}]) = 42.73 \pm 0.26 \text{ erg/s}$. Nine of the sources are from the Luo et al. (2017) catalogue in GOODS-S where the X-ray luminosity comes from the full (soft + hard) bands (0.5 – 7 Kev). The two remaining sources are from the Kocevski et al. (2018) catalogue in UDS for which the X-ray luminosity represents the hard band (2 – 10 kev). Whilst X-ray detections provide one way of identifying AGN activity in the ALMA – NIRSpec galaxies, as demonstrated by many high-redshift AGN studies (e.g. Lyu et al. 2022, 2024), it is crucial to use multi-wavelength tracers that capture the full multi-phase emission of AGN that can originate from both heavily dust obscured and unobscured regions (e.g. Padovani et al. 2017).

To further evaluate the presence of AGN activity in the ALMA – NIRSpec sample, we utilise the optical emission line diagnostics. In particular we calculate the $[O\text{III}]/H\beta$, $[S\text{II}]/H\alpha$, and $[N\text{II}]/H\alpha$ emission lines ratios, for which elevated line ratios can indicate the presence of harder ionizing spectrums and thus the presence of AGN activity (e.g. Kewley et al. 2001; Kauffmann et al. 2003) although as noted by many studies, high-metallicity star-bursting galaxies or low-metallicity AGN blur this demarcation (e.g. Gutkin et al. 2016; Strom et al. 2017; Garg et al. 2022; Agostino et al. 2023; Hirschmann et al. 2023).

For 14 of the ALMA – NIRSpec galaxies we have detections ($S/N > 3$) of the $[O\text{III}]\lambda 5008$ emission line of which 10 sources have further detections of the $H\beta$ emission-line (see Appendix B). For the four sources without $H\beta$ detections, we define 3σ upper limits on the $[O\text{III}]/H\beta$ line ratio if the NIRSpec spectra of the source covers the $H\beta$ emission line. In Figure 5, we construct

the Baldwin, Phillips & Terlevich (BPT) diagram (Baldwin et al. 1981), by correlating the observed (not dust-corrected) $[O\text{III}]/H\beta$ emission-line ratio with the $[N\text{II}]/H\alpha$ and $[S\text{II}]/H\alpha$ emission-line ratios. As indicated by the black arrow in Figure 5, which depicts the magnitude of a dust correction using a Calzetti et al. (2000) dust law with $A_V = 5$, the impact of the dust-correction on the line ratios is minimal given their spectral proximity. We note however the line ratios shown are slight upper limits as we do not account for stellar absorption of the Balmer lines, which has been shown to result in $\sim 2\%$ emission-line flux reduction of in post starburst galaxies with young stellar populations (e.g. González Delgado et al. 1999; Goto et al. 2003; Reddy et al. 2018).

In Figure 5, we further include the redshift matched comparison sample of star-forming galaxies from the CEERS and AURORA surveys. Compared to the CEERS and AURORA comparison samples at the same epoch, the ALMA – NIRSpec galaxies exhibit lower $[O\text{III}]/H\beta$ ratios with a median value of $\log_{10}([O\text{III}]/H\beta) = 0.11 \pm 0.08$ more comparable to local galaxies, which can potentially indicate a metal rich interstellar medium with low ionisation parameters (e.g. Steidel et al. 2014; Strom et al. 2017; Kashino & Inoue 2019). In Figure 5, we show the demarcation lines between SF and AGN from Kauffmann et al. (2003) at $z = 0$ as well as the redshift evolving division from Kewley et al. (2013) at $z = 2 - 3$. By evaluating the demarcation at the redshift of each ALMA – NIRSpec galaxies we establish the majority (94%) occupy the SF region at their respective epoch, with three galaxies exhibiting enhanced $[O\text{III}]/H\beta$ ratios

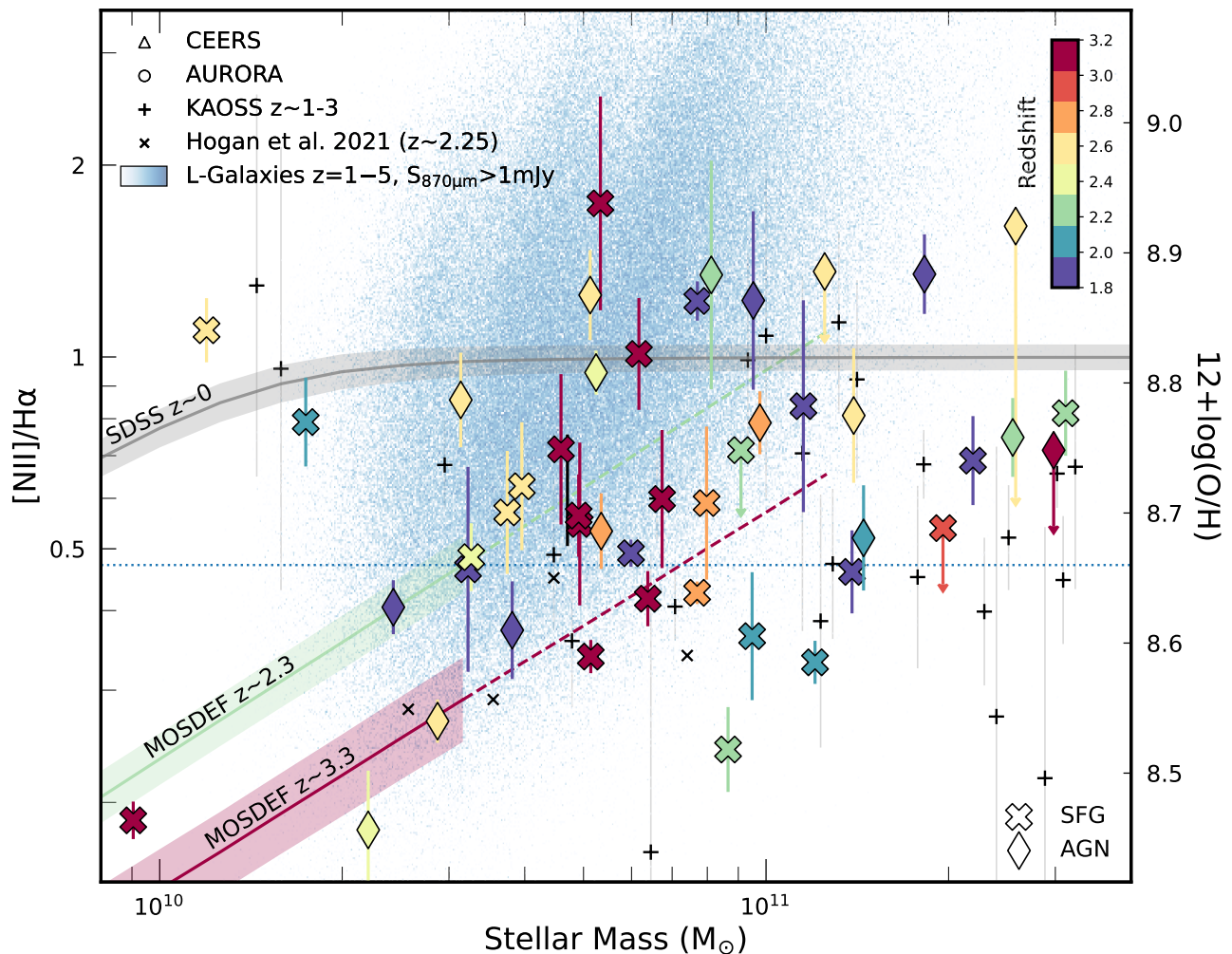


Fig. 6: Gas-phase metallicity, as derived from the $[\text{NII}]/\text{H}\alpha$ index using the [Bian et al. \(2018\)](#) strong-line calibrations, as a function of stellar mass for the ALMA – NIRSpec galaxies. Sources with $S/N < 3$ in their $[\text{NII}] 6584\text{\AA}$ emission-line are shown as limits. The horizontal dashed line indicates solar metallicity ([Asplund 2005](#), $12+\log(\text{O}/\text{H}) = 8.66$). We show comparison samples of typical star-forming galaxies at $z \sim 0$ from SDSS ([Curti et al. 2020](#)) (grey line), the MOSDEF Survey ([Sanders et al. 2021](#)) at $z \sim 2.3$ (green solid line) and $z \sim 3.3$ (red solid line), and a redshift matched sample of galaxies from the CEERS ([Shapley et al. 2023](#)) and AURORA Surveys ([Shapley et al. 2025](#)). We further compare to high-redshift observations of DSFGs from KAOSS at $z \sim 1-3$ ([Birkin 2022](#); [Birkin et al. 2024b](#)) and Herschel selected sources from [Hogan et al. \(2021\)](#) at $z \sim 2.25$, as well as far-infrared bright ($S_{870\mu\text{m}} > 1\text{mJy}$) at $z = 1-5$ galaxies (blue density) from the L-Galaxies simulation ([Araya-Araya et al. 2025a](#)). The ALMA – NIRSpec galaxies have higher gas-phase metallicity than the observational comparison samples at the same epoch, but comparable to predictions from L-Galaxies.

for their $[\text{NII}]/\text{H}\alpha$ line ratios, indicating their emission properties do not to purely originate from star formation activity alone. All three of these galaxies are detected in the [Luo et al. \(2017\)](#) 7Ms Chandra catalogue of GOODS-S and have intrinsic X-ray luminosities greater than 10^{42} erg/s.

Given not all ALMA – NIRSpec galaxies have detections of the $[\text{OIII}]/\text{H}\beta$ line ratio, we also investigate the distribution of $[\text{NII}]/\text{H}\alpha$ index in the sample, as shown by the grey histogram in Figure 5a. The ALMA – NIRSpec sample has a median value of $[\text{NII}]/\text{H}\alpha = 0.61 \pm 0.06$, which is below the typical threshold of $[\text{NII}]/\text{H}\alpha \gtrsim 0.8$ used to indicate AGN activity (e.g. [Wisnioski et al. 2018](#); [Leung et al. 2019](#); [Birkin et al. 2024a](#)) suggesting on average that their ionisation is not driven by AGN activity.

As well as optical emission-line ratio diagnostics, we can further use the profile of the rest-frame optical emission lines

to identify the presence of broad-line (Type-1) AGN in the ALMA – NIRSpec sample. Using the BIC parameter (Equation 1), from the emission-line fitting routine (see Sec 3.4.2), we can conduct a statistical analysis on the presence of broad line features. The ALMA – NIRSpec galaxies have a median $\text{H}\alpha$ FWHM of $328 \pm 27 \text{ km/s}^{10}$. Using the threshold of $\Delta\text{BIC}_{\text{H}\alpha, [\text{NII}], [\text{SII}]} < -10$ to indicate the presence of broad lines we identify nine galaxies (19%) that fulfil this criteria, of which five have X-ray counterparts with luminosities greater than 10^{42} erg/s. For these nine sources, with a median $\text{H}\alpha$ broad component FWHM of $1818 \pm 241 \text{ km/s}$, we report the narrow-line component emission-line ratios in all of the forthcoming analysis.

¹⁰ Excluding the 19 AGN from the sample, the median $\text{H}\alpha$ FWHM becomes $305 \pm 22 \text{ km/s}$

In total, we identify 19 (40%) of the ALMA–NIRSpec galaxies have indications of AGN activity either through X-ray counterparts, optical emission-line ratios or broad line components. Whilst we report the fraction of galaxies which show indications of AGN activity, we note given the sub-optimal placement of the NIRSpec slits for our sources (see Figure 1), there might be sources for which MSA shutter misses the central, core, region of the galaxy, that may harbour an AGN, thus we note this is a lower limit on AGN activity. Throughout the paper we highlight these 19 sources as AGN.

4.3. Gas-Phase Metallicity

Having identified the potential AGN contributions to the ALMA–NIRSpec galaxies emission, we now investigate the metallicity properties of the sample. Given the lack of coverage and low signal to noise ($<1\sigma$) of the $[\text{OII}] \lambda 4363$ emission-line in the NIRSpec spectra, it is not possible to derive the gas-phase metallicity using the ‘direct-method’ based on electron temperature (e.g. Pollock et al. 2025; Khostovan et al. 2025). However, we can use strong-line calibrations which give the relation between the higher signal-to-noise nebular lines and the gas-phase Oxygen abundance (e.g. Curti et al. 2020; Gillman et al. 2021, 2022).

In particular we adopt the relation from Bian et al. (2018) for the $[\text{NII}]/\text{H}\alpha$ index for which we have detections in 90% (43/48) of the sample. For the six remaining sources the $[\text{NII}] 6584\lambda$ emission-line has a $\text{S/N} < 3$ so we adopt a 3σ upper limit. The Bian et al. (2018) calibration is derived from stacked spectra of nearby galaxies whose $[\text{OIII}]/\text{H}\beta$ and $[\text{NII}]/\text{H}\alpha$ emission-line ratios place them in the same region of parameter space in the BPT diagram as those at higher redshift ($z \approx 2$). Specifically the gas-phase metallicity is given by,

$$12 + \log_{10}(\text{O}/\text{H}) = 8.82 + \log_{10}([\text{NII}]/\text{H}\alpha) \times 0.49 \quad (4)$$

As reported in Sanders et al. (2021), the $[\text{NII}]/\text{H}\alpha$ strong-line calibration of Bian et al. (2018) has an intrinsic ≈ 0.11 dex scatter. For the ALMA–NIRSpec galaxies, including the upper limits, we derive a median $[\text{NII}]/\text{H}\alpha$ ratio of $[\text{NII}]/\text{H}\alpha = 0.61 \pm 0.06$ with a 16–84th percentile range of $[\text{NII}]/\text{H}\alpha = 0.37 - 1.16$. This results in a median gas-phase metallicity of $12 + \log_{10}(\text{O}/\text{H}) = 8.71 \pm 0.02$, with a 16–84th percentile range of $12 + \log_{10}(\text{O}/\text{H}) = 8.61 - 8.85^{11}$. To understand if the sub-optimal placement of NIRSpec slits is biasing our results, we measure the gas-phase metallicity in a subsample of 28 galaxies whose ALMA–NIRSpec separation is $< 0''.1$, median separation of $0''.05$, identifying a consistently high metallicity of $12 + \log_{10}(\text{O}/\text{H}) = 8.76 \pm 0.03$.

In Figure 6, we plot the gas-phase metallicity, as a function of bagpipes derived stellar mass for the ALMA–NIRSpec galaxies, coloured by their spectroscopic redshift. We show the well established scaling relations derived for typical star-forming galaxies in the local Universe ($z \sim 0$) from SDSS (Curti et al. 2020), and the MOSFIRE Deep Evolution Field (MOSDEF; Kriek et al. 2015) Survey at $z \sim 2.3$ and $z \sim 3.3$ (Sanders et al. 2021), which on average are defined at lower stellar masses ($\log_{10}(M_* [M_\odot]) < 10.6$). We further include the redshift matched samples of typical star-forming galaxies from CEERS and AURORA as well as the SMGs from KAOSS (Birkin 2022; Taylor et al. prep) and Herschel selected sources from Hogan et al.

¹¹ Adopting the Pettini & Pagel (2004) strong-line calibrations results in a 0.16 dex higher metallicity.

(2021) at $z \sim 2.25$. Finally, we include the predictions for the sub-millimetre bright sources from the L-Galaxies SAM at $z = 1 - 5$ (Araya-Araya et al. 2025a,b).

On average we identify high gas-phase metallicities in the ALMA–NIRSpec galaxies, compared to other SFGs at the same epoch, comparable to the metallicities at $z \sim 0$. At the highest stellar masses, the sample is comparable to that reported in the KAOSS Survey ($12 + \log(\text{O}/\text{H}) \approx 8.75$; Birkin 2022), and in tentative agreement with extrapolations of the SFGs relations (dashed lines) defined at lower stellar masses. Below $10^{11} M_\odot$, the ALMA–NIRSpec galaxies exhibit high metallicities in agreement with the predictions from L-Galaxies. The majority of L-Galaxies sample falls below a stellar mass of $10^{11} M_\odot$, with a median stellar mass of $\log_{10}(M_* [M_\odot]) = 10.73$. As noted in Araya-Araya et al. (2025b), whilst the semi-analytical model matches the number counts of SMGs, there is an offset in the galaxy stellar mass function, with the model lacking the highest mass galaxies.

The super solar metallicities of the ALMA–NIRSpec galaxies is also in agreement with Kiyota et al. (2026) which identified $0.4 - 2 \times$ solar metallicity in 16 faint (median $\log_{10}(L_{\text{IR}} [L_\odot]) = 11.62 \pm 0.14$) ALMA detected sources from the ASPECS survey in GOODS-S with a median redshift and stellar mass of $z = 2.04 \pm 0.23$ and $\log_{10}(M_* [M_\odot]) = 10.31 \pm 0.20$. This is also in agreement with previous studies of the gas-phase metallicity in SMGs using the fine structure lines from Herschel-PACS observations (Wardlow et al. 2017) and targeted ALMA observations at higher redshift ($z > 4$), indicating the presence of a chemically evolved interstellar medium (Tadaki et al. 2019). Although, we note this is somewhat higher than the $0.9 \times$ solar metallicity reported by Suzuki et al. (2021) for $z > 3$ faint ALMA Band 6 ($S_{\text{B6}} = 0.11 \pm 0.15$ mJy) detected galaxies, which was derived using the metallicity calibrations of Curti et al. (2017) and not based on the $[\text{NII}]/\text{H}\alpha$ index.

4.4. Fundamental Metallicity Relation

To understand whether the ALMA–NIRSpec galaxies occupy the same fundamental metallicity relation (FMR) as typical SFGs, in Figure 7a we plot the offset in terms of gas-phase metallicity between the measured metallicity and that predicted by the plane, as parametrised by Curti et al. (2020) (see their Equation 5), for a given stellar mass and total star-formation rate of the ALMA–NIRSpec galaxies. We measure the same metallicity offset for the CEERS, AURORA, KAOSS and L-Galaxies samples. On average the ALMA–NIRSpec galaxies have an 0.11 ± 0.03 dex higher metallicity than predicted by the FMR, whilst being lower than the L-Galaxies model which at $z = 2 - 3$, has an average metallicity that is 0.22 dex higher than the FMR. The SFGs from CEERS and AURORA, for which we use the $\text{H}\alpha$ (dust corrected)¹² star-formation rate following the definition from Curti et al. (2020), are consistent with the relation with a median offset of -0.03 ± 0.02 dex.

Again, focussing on the brightest ($\log_{10}(L_{\text{FIR}} [L_\odot]) > 12.0$) and faintest ($\log_{10}(L_{\text{FIR}} [L_\odot]) < 11.5$) far-infrared ALMA–NIRSpec galaxies, we establish a median offset of 0.15 ± 0.03 dex and 0.08 ± 0.04 dex respectively. This indicates that at fixed stellar mass, for the high star-formation rates of the most far-infrared luminous ALMA–NIRSpec galaxies, the FMR predicts lower gas-phase metallicities than observed. This cautions against using the mass metallicity or fundamental

¹² Assuming a Calzetti et al. (2000) attenuation law and Case B recombination.

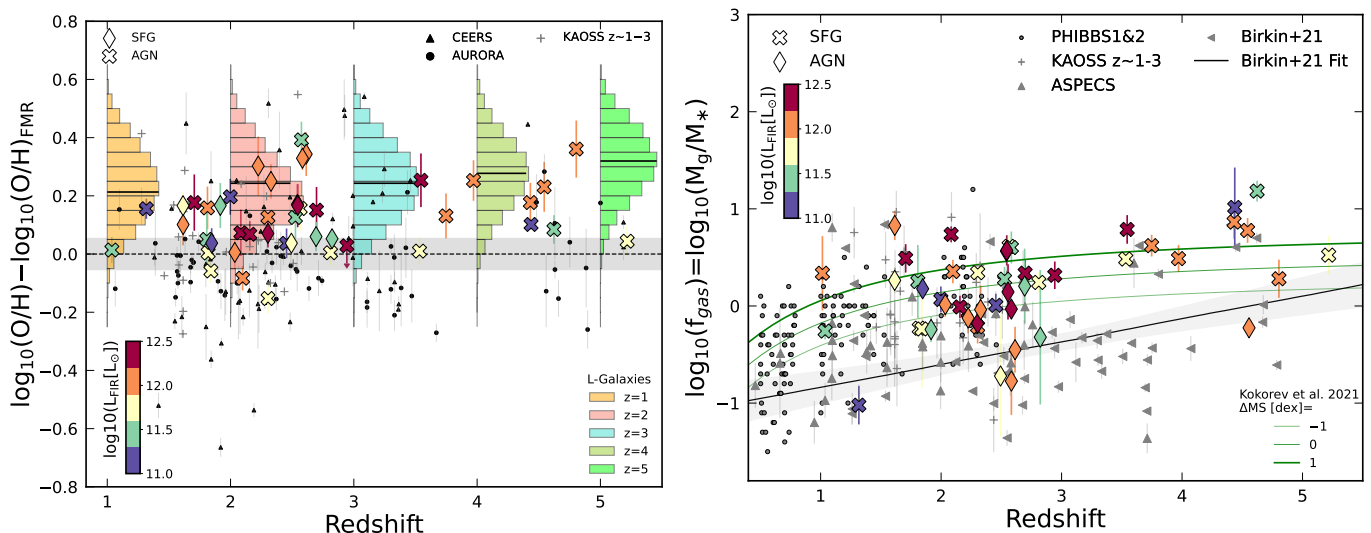


Fig. 7: **Left:** The metallicity offset to the fundamental metallicity relation (FMR) as defined by Curti et al. (2020), with the 0.05 dex uncertainty on the relation (grey shaded region). We include comparison samples from the CEERS and AURORA surveys (black points) (Shapley et al. 2023, 2025) as well as sub-millimetre bright (>1 mJy) galaxies in the L-Galaxies simulation (histograms) at $z=1-5$ (Araya-Araya et al. 2025a), with the median at each redshift snapshot indicated by the black line. On average the ALMA – NIRSpec galaxies show a 0.11 ± 0.03 dex elevation in metallicity compared to the FMR, which is slightly lower than the predictions from L-Galaxies. **Right:** Gas Fraction (M_{g}/M_{\star}) as function redshift for the ALMA – NIRSpec galaxies coloured by their total specific star-formation rate. We include comparison samples of SFGs from the PHIBBS (Tacconi et al. 2018) and ASPECS (Boogaard et al. 2020) surveys, SMGs with CO-derived gas masses from Birkin et al. (2021) and SMGs with metallicity derived gas masses from KAOSS (Birkin 2022; Birkin et al. 2024b). We further over plot the best fitting relation from Birkin et al. (2021) (black line). The ALMA – NIRSpec galaxies show elevated gas fractions compared to the CO-detected samples, more consistent with the main sequence scaling from Kokorev et al. (2021).

metallicity relations to infer the metallicity, as is often routine in studies of luminous far-infrared galaxies, where direct metallicity measurements are unavailable (e.g. Magdis et al. 2012; Liu et al. 2019; Donevski et al. 2020; Gómez-Guijarro et al. 2022)

The elevated metallicity could be explained by a lack inflow of pristine gas into the galaxies, that would normally dilute the metal content of the interstellar medium, although this would also result in a short-lived star-formation episode, with no renewed fuel for star formation. An alternative scenario is that the metal enrichment and dust production in most far-infrared luminous ALMA – NIRSpec galaxies, is on average, higher than typical main-sequence galaxies, but it is unlikely to be the galaxies have higher gas fractions, given this would place them back on the fundamental metallicity relation.

To explore these two scenarios, we now investigate the gas fraction of the ALMA – NIRSpec galaxies. Using the gas-phase metallicity and the dust mass we can infer the gas fraction (M_{g}/M_{\star}) of the ALMA – NIRSpec galaxies from the relations between dust to gas ratio (DtG) and metallicity. We use the non-redshift evolving, metallicity dependent, dust to gas ratio from Popping et al. (2022), given by

$$\log_{10}(\text{DtG}) = 1.30 \times (12 + \log_{10}[\text{O}/\text{H}]) - 13.72 \quad (5)$$

For the ALMA – NIRSpec sample, we measure a median dust to gas ratio of $\log_{10}(\text{DtG}) = -2.37 \pm 0.03$ with a 16th – 84th percentile range of $\log_{10}(\text{DtG}) = -2.38$ to -2.34 . In Figure 7b, we show the gas fraction of the ALMA – NIRSpec galaxies as function of redshift, coloured by far-infrared luminosity. We include other literature samples of SFGs from the IRAM Plateau de Bure high-z blue sequence CO 3-2 survey (PHIBBS; Tacconi et al. 2013, 2018), the ASPECS survey (Walter et al.

2016), as well as CO-selected SMGs from Birkin et al. (2021) and, $\text{H}\alpha$ -detected SMGs from KAOSS (Birkin 2022; Taylor et al. prep), for which we use Equation 5 to derive the gas fraction. On average, the ALMA – NIRSpec galaxies have higher gas fractions than the relation derived from Birkin et al. (2021), with a median gas fraction of $\log_{10}(M_{\text{g}}/M_{\star}) = 0.26 \pm 0.08$ with a 16th – 84th percentile range of $\log_{10}(M_{\text{g}}/M_{\star}) = -0.23$ to 0.62 , more consistent with the observationally derived main sequence scaling from Kokorev et al. (2021) (green lines in Figure 7b), although we note this is derived using a different metallicity and gas to dust ratio calibration. This implies the median depletion timescale ($t_{\text{depl}} = M_{\text{g}}/\text{SFR}$), for the ALMA – NIRSpec sample is $t_{\text{depl}}[\text{Gyr}] = 0.77 \pm 0.08$, which is higher than the $t_{\text{depl}}[\text{Gyr}] = 0.21 \pm 0.04$ reported by Birkin et al. (2021) for CO-selected SMGs. We note, in part this is likely driven by the broad range of far-infrared luminosity in the ALMA – NIRSpec galaxies, in addition to the lower, metallicity inferred, dust to gas ratio of our sample, compared to the typically adopted Milky Way value of $\log_{10}(\text{DtG}) = -2.0$ (e.g. Swinbank et al. 2014; Birkin 2022)

An alternative approach to deriving the gas mass of high-redshift galaxies, is to measure their CO line luminosity, and convert this to a gas mass using the CO-to- H_2 conversion factor (α_{CO}) (e.g. Greve et al. 2005; Bothwell et al. 2013; Tacconi et al. 2018; Birkin et al. 2021; Nicandro Rosenthal et al. 2026). The choice of α_{CO} has a significant impact on the derived gas mass and is a strong function of metallicity, with values varying from $\alpha_{\text{CO}} = 1$, consistent with local merging (U/LIRGs) galaxies, to $\alpha_{\text{CO}} = 3.6$, consistent with local disk galaxies (see Bolatto et al. 2013 for a full review). Whilst we do not have measurements of the CO line luminosity for the ALMA – NIRSpec sample, we can use the gas-phase metallicity to infer α_{CO} . We adopt the relation

from Magdis et al. (2012), that relates the gas-phase metallicity to α_{CO} of the form,

$$\log_{10}(\alpha_{\text{CO}}) = \alpha \times (12 + \log_{10}[\text{O}/\text{H}]_{\text{PP04}}) + \beta \quad (6)$$

where the gas-phase metallicity is derived using the Pettini & Pagel (2004) $[\text{NII}]/\text{H}\alpha$ strong-line calibration, $\alpha = -1.39 \pm 0.3$ and $\beta = 12.8 \pm 2.2$. For the ALMA–NIRSpec sample we derive a median $12 + \log_{10}[\text{O}/\text{H}]_{\text{PP04}} = 8.76 \pm 0.02$, which is slightly higher than that derived using Equation 4. Using Equation 6 we thus derive a median $\alpha_{\text{CO}} = 4.12 \pm 0.31$ with a 16th–84th percentile range of $\alpha_{\text{CO}} = 2.73$ –6.31. We further identify no significant difference between far-infrared bright and faint galaxies with median values CO-to-H₂ conversion factor of $\alpha_{\text{CO}} = 3.74 \pm 0.40$ and $\alpha_{\text{CO}} = 4.73 \pm 1.18$. This implies that the CO-to-H₂ conversion factor of our sample is more consistent with local disk galaxies (e.g. Leroy et al. 2011; Chiang et al. 2024), and does not have strong dependence on far-infrared luminosity, or in fact main sequence offset. Adopting an $\alpha_{\text{CO}} \simeq 4$ for the Birkin et al. (2021) sample of CO-selected SMGs, would move them to higher gas fractions, more aligned with the ALMA–NIRSpec sample. We note however that this inference of α_{CO} is purely based on metallicity, which has been demonstrated to likely be an over simplification, with α_{CO} having further dependences on the density and pressure of the interstellar medium (e.g. Narayanan et al. 2012; Accurso et al. 2017; Madden et al. 2020; Bisbas et al. 2025).

4.5. Electron Density

In addition to the gas-phase metallicity and gas fractions, we can constrain the electron density within interstellar medium of the ALMA–NIRSpec galaxies, using the $[\text{SII}]$ doublet ratio, allowing a physically motivated interpretation of the ionised interstellar medium conditions. For the sample of ALMA–NIRSpec sample, we obtain detections ($\text{S/N} > 3$) of the $[\text{SII}] \lambda 6716$ emission in 17% (8/48) and detections of the $[\text{SII}] \lambda 6731$ emission line in 31% (15/48) sources. For those sources with $\text{S/N} < 3$ in either $[\text{SII}]$ line, we define a 3σ upper limit, whilst for 30 sources with $\text{S/N} < 3$ in both $[\text{SII}]$ lines, we do not derive the doublet ratio and electron density. We derive a median doublet ratio of $[\text{SII}] \lambda 6716 / [\text{SII}] \lambda 6731 = 0.98 \pm 0.05$ and 16–84th percentile range of $[\text{SII}] \lambda 6716 / [\text{SII}] \lambda 6731 = 0.77$ –1.30.

In Figure 8a we plot the observed $[\text{SII}]$ doublet ratio as a function of spectroscopic redshift for the ALMA–NIRSpec galaxies as well as the CEERS and AURORA redshift matched samples, highlighting the region in which the ratio is sensitive to the electron density. The ALMA–NIRSpec galaxies exhibit slightly lower $[\text{SII}]$ doublet ratios to the SFGs from CEERS and AURORA at the same epoch, which have a median value of $[\text{SII}] \lambda 6716 / [\text{SII}] \lambda 6731 = 1.26 \pm 0.02$. Previous studies of high-redshift SFGs have investigated the correlation between electron density and specific star-formation rate, often reporting mixed results (e.g. Kashino & Inoue 2019; Davies et al. 2021; Gillman et al. 2022; Topping et al. 2025). In Figure 8a, we colour both the ALMA–NIRSpec galaxies and comparison samples by total specific star-formation rate (sSFR), where SFR_{tot} is defined as $\text{H}\alpha$ dust uncorrected SFR plus SFR_{FIR} . We identify no clear correlation between $[\text{SII}]$ doublet ratio and sSFR.

Following the prescription of Kewley et al. (2019b), based on the mappings v5.1¹³ photoionisation models, we can convert the observed $[\text{SII}]$ doublet ratio to an electron density. For

the ALMA–NIRSpec galaxies we derive a median electron density of $\log_{10}(n_e)[\text{cm}^{-3}] = 2.53 \pm 0.07$ with a 16–84th percentile range of $\log_{10}(n_e)[\text{cm}^{-3}] = 2.05$ –2.81. In Figure 8b, we show the electron density of the ALMA–NIRSpec galaxies, derived from the $[\text{SII}]$ doublet ratio as a function of spectroscopic redshift, compared to the CEERS and AURORA samples as well as literature studies of SFGs across a broad range of redshift from SAMI ($z \sim 0$; Davies et al. 2021), KROSS ($z \sim 1$; Swinbank et al. 2019), FMOS ($z \sim 1.6$; Kashino et al. 2017), MOSDEF ($z \sim 2.3$; Sanders et al. 2016) and, KMOS-3D ($z \sim 2.6$; Davies et al. 2021) surveys. We include the evolution of electron density with redshift from Abdurro'uf et al. (2024) of $n_e \propto (1+z)^{1.2}$, which predicts a median value of $\log_{10}(n_e)[\text{cm}^{-3}] = 2.41 \pm 0.03$ and 16–84th percentile range of $\log_{10}(n_e)[\text{cm}^{-3}] = 2.01$ –2.79, across the redshift range of the ALMA–NIRSpec sample ($z = 1.04$ –5.22), consistent with the measured value. We note the large fraction of lower limits in Figure 8b which consistently fall above the relation from Abdurro'uf et al. (2024), potentially indicate higher signal to noise spectra could reveal elevated electron densities.

We further find no strong correlation with far-infrared luminosity in the ALMA–NIRSpec galaxies, indicating consistent electron densities independent of far-infrared emission, consistent with recent results from Kiyota et al. (2026). We note that the electron density, and those of the comparison samples, are purely derived from rest-frame optical emission lines, which is not equivalent to that derived from far-infrared fine structure lines (e.g. Lee et al. 2019; Zhang et al. 2019) which tend to find lower electron densities ($\log_{10}(n_e)[\text{cm}^{-3}] < 2$). This is attributed to the fine structure lines being sensitive to different densities and physical conditions within the interstellar medium, than the optical diagnostics (e.g. Schimek et al. 2024; Harikane et al. 2025; Usui et al. 2025).

4.6. Ionisation Parameter

We can further constrain the ionisation conditions of the interstellar medium of the ALMA–NIRSpec galaxies through the ionisation parameter (U), which represents the ratio of the density of ionising photons to the density of hydrogen atoms (Osterbrock & Ferland 2006). Of the rest-frame optical emission lines detected in the NIRSpec spectra, the O_{32} strong-line ratio ($[\text{OIII}] 5007\lambda / [\text{OII}] 3727,9\lambda\lambda$) is sensitive to the ionisation parameter, where higher ratios O_{32} , at fixed metallicity and interstellar medium pressure, indicate a more highly ionised nebula.

Utilising the numerical prescription from the mappings v5.1 photoionisation code (Kewley et al. 2019a), and the gas-phase metallicity for each source as given by Equation 4, at a constant interstellar medium pressure of $\log_{10}(P/k) = 5^{14}$ we can derive the ionisation parameter for the ALMA–NIRSpec galaxies. In 25% (12/48) of the sample we have coverage of the $[\text{OII}] 3727,9\lambda\lambda$ emission line, with five sources having $\text{S/N} < 3$, thus we define a 3σ upper limit. Given the wavelength separation of the $[\text{OII}] 3727,9\lambda\lambda$ and $[\text{OIII}] 5007\lambda$ emission lines, to derive an accurate O_{32} index, and thus ionisation parameter, it is critical to dust correct both emission lines. However, given the lack of coverage of the $\text{H}\beta$ emission-line in the ALMA–NIRSpec galaxies, and thus poorly constrained nebular attenuation, we first derive the observed (dust-uncorrected) ionisation parameter for the sources. This represents an upper limit on the intrinsic ionisation parameter of the sources, given a nebula dust

¹³ <https://mappings.anu.edu.au/>

¹⁴ We note a higher pressure would result in higher ionisation parameter for a given metallicity, see Kewley et al. (2019a) for details.

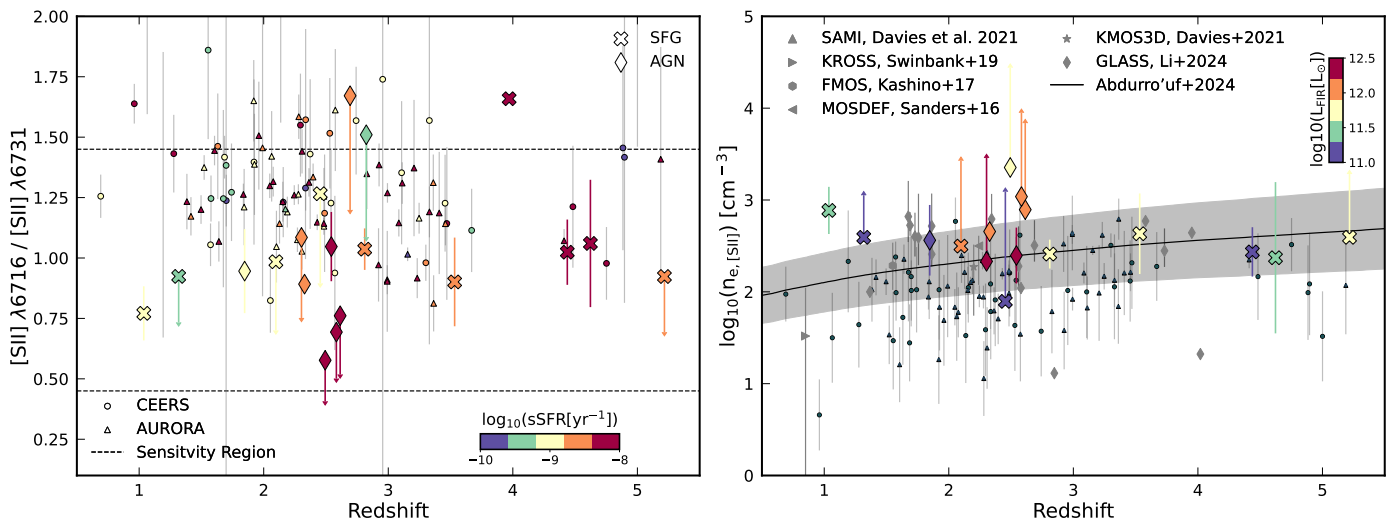


Fig. 8: **Left:** [SII] doublet emission-line ratio as function of spectroscopic redshift for the ALMA – NIRSpec sample coloured by specific star-formation rate (sSFR). Sources with $S/N < 3$ in either [SII] emission-lines are shown as limits. We show comparison samples of typical star-forming galaxies from the CEERS Survey [Shapley et al. \(2023\)](#) (circles) and AURORA survey [Shapley et al. \(2025\)](#) (triangles). We further indicate the sensitivity region (black dashed lines) of the [SII] line ratio to the electron density ([Kewley et al. 2019b](#)). The ALMA – NIRSpec sample exhibits slightly lower [SII] doublet emission-line ratios to the lower mass SFGs samples from CEERS and AURORA, with no clear dependence on sSFR. **Right:** The [SII] derived electron density, using the mappings v5.1 photoionisation code ([Kewley et al. 2019b](#)), as a function of spectroscopic redshift, with the ALMA – NIRSpec galaxies coloured by dust mass. The grey solid line indicates the typical evolution of star-forming galaxies ($n_e \propto (1+z)^{1.2}$) from [Abuduro'uf et al. \(2024\)](#). The electron density of the ALMA – NIRSpec galaxies are consistent with typical star-forming galaxies, with no strong correlations with specific star-formation rate or far-infrared luminosity.

correction would act to reduce the O_{32} index, and thus reduce the ionisation parameter further.

We derive a median (dust-uncorrected) O_{32} index of $O_{32} = 0.70 \pm 0.10$ with a 16th – 84th of $O_{32} = 0.54 - 1.13$ which corresponds to a median (dust-uncorrected) ionisation parameter of $\log_{10}(U) = -2.84 \pm 0.06$ with a 16 – 84th percentile range of $\log_{10}(U) = -2.96$ to -2.63 . This is much lower than expected given the high star formation rates of DSFGs (e.g. [Casey et al. 2014](#); [Dudzevičiūtė et al. 2020](#)) and is comparable to that derived for the typical star-forming galaxies at the same epoch (e.g. [Sanders et al. 2016](#); [Kaasinen et al. 2018](#); [Reddy et al. 2023](#)).

It is well known for SFGs, that there is strong correlation between ionisation parameter and $H\alpha$ star-formation rate surface density ($\Sigma_{H\alpha, SFR}$), whereby galaxies with higher star formation rate surface densities have an increased ionisation parameter i.e. a greater amount of ionising photons to the density of hydrogen atoms in the interstellar medium. (e.g. [Nakajima & Ouchi 2014](#); [Kaasinen et al. 2018](#); [Papovich et al. 2022](#); [Reddy et al. 2023](#)). However, whether this relation holds true for dust-obscured and star-bursting systems is unknown. In Figure 9 we plot the observed (not dust corrected) ionisation parameter (U), as derived from the O_{32} index as a function of $H\alpha$ star-formation rate surface density ($\Sigma_{H\alpha, SFR}$) derived using the ALMA – NIRSpec galaxies optical sizes (see Sec. 3.3), as well as the parametric scaling derived by [Reddy et al. \(2023\)](#) for the CEERS survey.

We further show the individual (dust-corrected) measurements from the redshift matched sample of CEERS galaxies, derived using the same methodology. For the CEERS galaxies we further utilise the observed $H\alpha/H\beta$ ratio to dust correct the emission line fluxes, and thus derive a dust corrected ionisation parameter and $H\alpha$ star-formation rate surface density. Assuming Case B recombination at an electron temperature of

$T_e = 10,000$ K and an electron density of $n_e = 100 \text{ cm}^{-3}$ ([Osterbrock & Ferland 2006](#))¹⁵, the nebular dust attenuation derived from the Balmer decrement is defined as,

$$A_{V, \text{gas}} = R_V E(B - V) = \frac{R_V}{0.4(K_{H\beta} - K_{H\alpha})} \times \log_{10}\left(\frac{H\alpha/H\beta}{2.86}\right) \quad (7)$$

where K_λ denotes the magnitude of extinction at a given wavelength from the extinction curve, and R_V is the total-to-selective extinction ratio. For the CEERS sample the median Balmer decrement is $H\alpha/H\beta = 3.22 \pm 0.16$ and thus with $R_V = 4.05$ the median $A_V = 0.6 \pm 0.1$

For the ALMA – NIRSpec galaxies, given the inconsistent coverage of the $H\beta$ emission line we can not derive the dust correction for all sources. The ALMA – NIRSpec galaxies scatter about the relation indicating a similar trend maybe present in DSFGs. Previous studies of star-forming galaxies have further identified that galaxies with high ionisation parameters exhibit systematically lower electron densities. In Figure 9 we colour both the CEERS sample and ALMA – NIRSpec galaxies by their [SII] derived electron density, although given the low number statistics, it is not clear whether the ALMA – NIRSpec galaxies follow this trend.

As indicated by the black arrow in Figure 9, even with an $A_{V, \text{Nebular}} = 1$, there is a strong correction on both the ionisation parameter and $H\alpha$ star-formation rate surface density when the dust content is taken into account. For nine sources, we have detections of both the O_{32} ratio and the $H\beta$ line with a median Balmer decrement of $H\alpha/H\beta = 5.84 \pm 0.75$, thus adopting a [Calzetti et al. \(2000\)](#) attenuation curve with $R_V = 4.05$ and electron density of $n_e = 100 \text{ cm}^{-3}$ (consistent with Figure 8), we

¹⁵ We note at fixed electron temperature, adjusting the electron density to observed value does not alter the intrinsic Balmer decrement

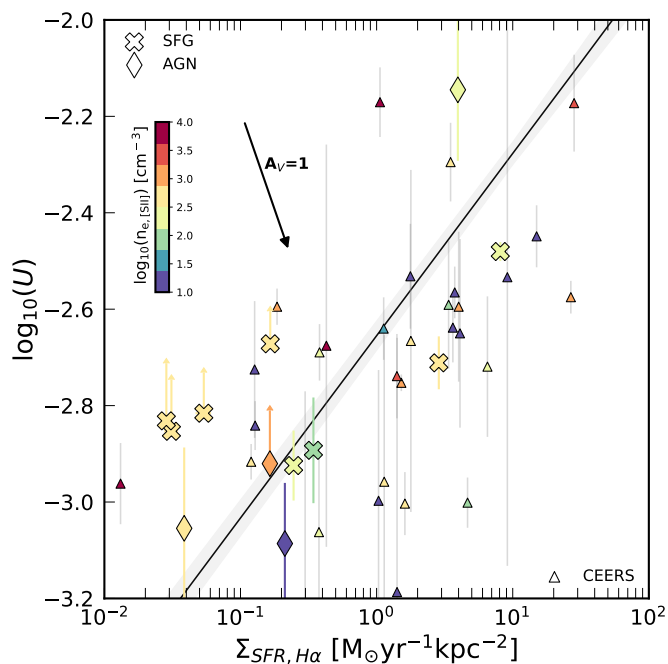


Fig. 9: Ionisation parameter (U), as derived from the O_{32} strong-line ratio, as a function of $H\alpha$ star-formation rate surface density. For the ALMA – NIRSpec galaxies this represents the observed (dust-uncorrected) values whilst for the CEERS sample we show the intrinsic (dust-corrected) values. We colour the galaxies by $[SII]$ derived electron density and show the parametric fit from Reddy et al. (2023) for the CEERS survey of the form $\log_{10}(U) = (0.378 \pm 0.021) \times \log_{10}(sSFR) - (2.655 \pm 0.011)$. The black arrow indicates the impact of dust attenuation with $A_V = 1$. The observed (dust-uncorrected) values of the ALMA – NIRSpec galaxies are consistent with dust-corrected CEERS galaxies, although with low number statistics.

derive a nebular dust attenuation of $A_{V, Nebular} = 2.55 \pm 0.43$ ¹⁶. Whilst this is for only a subset of sources we expect $A_{V, Nebula} > 1$ in the majority ALMA – NIRSpec galaxies, given the expectation of higher nebular attenuation than stellar attenuation, especially in massive galaxies (e.g. Calzetti et al. 2000; Reddy et al. 2020; Lorenz et al. 2026) and from Table C.1, the median bagpipes derived stellar attenuation of the sample is $A_{V, Stellar} = 2.23 \pm 0.14$.

For the nine sources with detections of both the O_{32} ratio and $H\beta$ line we establish a median dust-corrected ionisation parameter of $\log_{10}(U) = -3.93 \pm 0.37$. However, we note this is an upper limit given the photoionization models presented in Kewley et al. (2019a) are not defined below $\log_{10}(U) < -3.9$. This would result in the ALMA – NIRSpec galaxies lying below the relation of typical SFGs in Figure 9, with lower ionisation parameters than implied by their high star-formation rate surface densities (e.g. Kashino & Inoue 2019). The dust corrected ionisation parameter is derived assuming the ALMA – NIRSpec galaxies have a similar dust attenuation law to Calzetti et al. (2000) which many studies have suggested otherwise (e.g. Kriek & Conroy 2013; Popping et al. 2017; Hamed et al. 2023; Sun et al. 2026). Furthermore, the optical line O_{32} ratios dependence on the ionisation parameter is a strong function of interstellar medium pres-

sure and only traces the less obscured, ionised, regions of the galaxies, in contrast to the far-infrared fine structure lines which are sensitive to deeply obscured star formation (e.g. Rigopoulou et al. 2018b; Decarli & Díaz-Santos 2025). The optical line diagnostics further have potential contamination from diffuse ionised gas which local studies have shown can have significantly lower the ionisation parameter (e.g. Zhang et al. 2017; Belfiore et al. 2022).

5. Conclusions

We present a spectroscopic analysis of a comprehensive, but inhomogeneously selected, sample identified from archival ALMA observations (Liu et al. 2019; Adscheid et al. 2024; Lee et al. 2025). Utilising the NIRSpec median resolution (or higher) observations from DJA, from an initial sample of 121 galaxies, we built a final sample of 48 ALMA – NIRSpec galaxies with robust ($>3\sigma$) ALMA counterparts and rest-frame optical spectroscopy that captures the $H\alpha$ emission-line. We determine the samples multi-wavelength (near-infrared and far-infrared) SED properties as well as defining the galaxies interstellar medium properties from rest-frame optical diagnostics. Our main conclusions are:

- **Star Formation and Dust Content** On average the ALMA – NIRSpec sample lies 0.32 ± 0.07 dex above the main sequence with the highest infrared luminosity galaxies lying at ≥ 0.5 dex, consistent with other far-infrared bright galaxies from ASUDS (Dudzevičiūtė et al. 2020) and KAOS (Birkin et al. 2024a), as well as the most massive, sub-millimetre bright galaxies, from L-Galaxies (Araya-Araya et al. 2025b). The ALMA – NIRSpec galaxies have median dust fraction of $\log_{10}(M_d/M_*) = -2.20 \pm 0.08$, which as shown in Figure 4, is consistent with other the sub-millimetre bright galaxy samples at a median redshift of $z = 2.5$, but the sample exhibits higher dust fractions at higher redshift.
- **Ionisation Origin** The majority of the sample (29/48) show no signs of AGN activity in terms of X-ray counterparts, optical emission-line ratios (Figure 5) with an average $[NII]/H\alpha$ index of $[NII]/H\alpha = 0.61 \pm 0.06$, or broad emission line features with an average $H\alpha$ FWHM of 328 ± 27 km/s. Of the 19 galaxies flagged as AGN, 15 sources have X-ray counterparts $> 10^{42}$ erg/s, 3 occupy the AGN region of the BPT diagram at their epoch, based on the Kewley et al. (2013) redshift evolving demarcation, and nine galaxies show improved emission-line fits ($\Delta BIC_{H\alpha, [NII], [SII]} < -10$) when a broad component is included, with a median $H\alpha$ broad FWHM of 1818 ± 241 km/s. Although, we note this is a lower limit on the AGN activity in the sample given the stochastic placement of NIRSpec/MSA slits that can miss the central, core, regions of galaxies, which may harbour AGN.
- **Metallicity and Gas Fraction** We identify super solar, gas-phase metallicities in ALMA – NIRSpec galaxies compared to typical SFGs at the same epoch and other $H\alpha$ -detected high-redshift SMG samples, with a median gas-phase metallicity of $12 + \log_{10}(O/H) = 8.71 \pm 0.02$ derived from the $[NII]/H\alpha$ index using the Bian et al. (2018) calibration. For far-infrared bright ($\log_{10}(L_{IR}[L_\odot]) > 12.0$) galaxies we derive a median metallicity offset to the Curti et al. (2020) fundamental metallicity plane of 0.15 ± 0.03 dex, suggesting DSFGs do not follow the same equilibrium between metal enrichment and star formation as more typical, less dust-obscured, galaxies. Using the metallicity dependent gas-to-dust ratio from Popping et al. (2017), we derive a median gas

¹⁶ We note this is an upper limit on the nebular attenuation as we do not account for potential stellar absorption from older stellar populations.

fraction of $\log_{10}(M_g/M_*) = 0.26 \pm 0.08$, which is elevated with respect to other studies of bright SMGs at the same epoch, suggesting a strong connection between far-infrared luminosity, metal content and gas fraction.

- **Electron Density** From an analysis of the [SII] emission-line doublet ratio, and adopting the photoionization modelling from Kewley et al. (2019b), we established a median electron density for the ALMA – NIRSpec sample of $\log_{10}(n_e)[\text{cm}^{-3}] = 2.53 \pm 0.07$, consistent with star-forming galaxies at the same epoch and the cosmic evolution of electron density as parametrised by Abdurro'uf et al. (2024), with no strong correlation with specific star-formation rate or far-infrared luminosity.
- **Ionisation Parameter** Utilising the sensitivity of the O_{32} index to the ionisation parameter (U), and following the prescriptions of Kewley et al. (2019a), we derive a median (dust-uncorrected) ionisation parameter of $\log_{10}(U) = -2.84 \pm 0.06$ for a subsample of the ALMA – NIRSpec galaxies, comparable to the dust-corrected ionisation parameters of the typical star-forming galaxies at the same epoch. Finally, we derive an upper limit on the dust-corrected ionisation parameter ($\log_{10}(U) = -3.93 \pm 0.37$) suggesting the far-infrared detected galaxies fall below the ionisation parameter to $H\alpha$ derived star-formation rate relation established for star-forming galaxies when using optical line diagnostics and a Calzetti et al. (2000) dust attenuation law.

Despite the dust rich nature of the ALMA – NIRSpec sample, our analysis indicates that the electron density, as derived from optical line diagnostics, are consistent with the broader population of star-forming galaxies at the same epoch. However, the inferred ionisation parameters are lower than expected given the rate of star formation rates of the sample, whilst the brightest far-infrared sources exhibit elevated gas-phase metallicities relative to their stellar masses and star-formation rates. These findings suggest the ALMA – NIRSpec sources do not maintain the same equilibrium between metal enrichment, dust production and star formation as more typical, less dust-obscured, galaxies. Caution is therefore needed when adopting the mass metallicity to infer the metallicity of DSFGs.

While our study demonstrates the power of NIRSpec/MSA spectroscopy in detecting the rest-frame optical emission line features in the previously inaccessible parameter space of high-redshift DSFGs, limitations remain. Non-optimum placement of NIRSpec slits and heterogenous signal to noise across the archival observations introduces potential biases that affect our derived properties. Future higher signal to noise NIRSpec observations will be essential to robustly characterise the multi-phase interstellar medium of dust-obscured galaxies.

6. Data Availability

A machine readable table of the full 138 sources with NIRSpec derived spectroscopic redshifts and ALMA detections, in addition to the mercurius MCMC fitting results for the final sample, can be found on this [link](#).

Acknowledgements. The observations analysed in this work are made with the NASA/ESA/CSA James Webb Space Telescope (DOI: 10.17909/z7p0-8481). We thank Ryan Sanders and Alice Shapley for sharing the NIRSpec properties for the CEERS and AURORA surveys. We acknowledged financial support from the Cosmic Dawn Center (DAWN), funded by the Danish National Research Foundation (DNRF) under grant DNRF140. FV, KI, AP acknowledges support from the Independent Research Fund Denmark (DFF) under

grant 3120-00043B. BG and CH acknowledge support from Villum Fonden under project grant 53120. PA-A acknowledge support from the Independent Research Fund Denmark (DFF) under grant 4251-00086B. SJ acknowledges the Villum Fonden research grants 37440 and 13160. PFW acknowledges funding through the National Science and Technology Council grants 113-2112-M-002-027-MY2. DC is supported by research grant PID2024-156100NB-C21 financed by MICIU/AEI/10.13039/501100011033 / FEDER, EU., and the research grant CNS2024-154550 funded by MI-CIU/AEI/10.13039/501100011033. TK acknowledges support from JSPS grant 25KJ1331. FR acknowledges support from the Dutch Research Council (NWO) through the Veni grant VI.Veni.222.146. SF acknowledges support from the Dunlap Institute, funded through an endowment established by the David Dunlap family and the University of Toronto. JRW acknowledges that support for this work was provided by The Brinson Foundation through a Brinson Prize Fellowship grant. MO acknowledges support from JSPS KAKENHI Grant Number JP25K07361. ML acknowledges support from the European Union's Horizon 2020 research and innovation program under the Marie Skłodowska-Curie grant agreement No 101107795 and by the DeIC National HPC (DeIC-DTU-N2-2024057).

References

- Abdurro'uf et al., 2024, *ApJ*, 973, 47
Accurso G., et al., 2017, *MNRAS*, 470, 4750
Adscheid S., et al., 2024, *A&A*, 685, A1
Agostino C. J., Salim S., Boquien M., Janowiecki S., Salas H., Couto G. S., 2023, *MNRAS*, 526, 4455
Alaghband-Zadeh S., et al., 2012, *MNRAS*, 424, 2232
Algera H. S. B., et al., 2023, *MNRAS*, 518, 6142
Amvrosiadis A., et al., 2023, *arXiv e-prints*, p. [arXiv:2312.08959](#)
Aravena M., et al., 2016, *ApJ*, 833, 68
Araya-Araya P., et al., 2025a, *arXiv e-prints*, p. [arXiv:2509.26646](#)
Araya-Araya P., Cochrane R. K., Hayward C. C., Sodr e Jr. L., Yates R. M., van Daalen M. P., Vicentin M. C., 2025b, *MNRAS*, 542, 2808
Asplund M., 2005, *ARA&A*, 43, 481
Bakx T. J. L. C., et al., 2026, *arXiv e-prints*, p. [arXiv:2601.09780](#)
Baldwin J. A., Phillips M. M., Terlevich R., 1981, *PASP*, 93, 5
Barbary K., Boone K., McCully C., Craig M., Deil C., Rose B., 2016, Kbarbary/Sep: V1.0.0, Zenodo, [doi:10.5281/zenodo.159035](#)
Baugh C. M., Lacey C. G., Frenk C. S., Granato G. L., Silva L., Bressan A., Benson A. J., Cole S., 2005, *MNRAS*, 356, 1191
Belfiore F., et al., 2022, *A&A*, 659, A26
Bertin E., 2011, in Evans I. N., Accomazzi A., Mink D. J., Rots A. H., eds, *Astronomical Society of the Pacific Conference Series Vol. 442, Astronomical Data Analysis Software and Systems XX*. p. 435
Bertin E., Arnouts S., 1996, *A&AS*, 117, 393
Bian F., Kewley L. J., Dopita M. A., 2018, *ApJ*, 859, 175
Bing L.-J., et al., 2024, *A&A*, 683, A232
Birkin J. E., 2022, PhD thesis, Durham University, UK
Birkin J. E., et al., 2021, *MNRAS*, 501, 3926
Birkin J. E., et al., 2024a, *MNRAS*, 531, 61
Birkin J. E., et al., 2024b, *MNRAS*, 531, 61
Bisbas T. G., et al., 2025, *A&A*, 697, A115
Blain A. W., Smail I., Ivison R. J., Kneib J.-P., Frayer D. T., 2002, *Phys. Rep.*, 369, 111
Bodansky S., et al., 2025, *arXiv e-prints*, p. [arXiv:2507.19472](#)
Bolatto A. D., Wolfire M., Leroy A. K., 2013, *ARA&A*, 51, 207
Boogaard L. A., et al., 2020, *ApJ*, 902, 109
Boogaard L. A., et al., 2023, *arXiv e-prints*, p. [arXiv:2308.16895](#)
Bothwell M. S., et al., 2013, *MNRAS*, 429, 3047
Brammer G., 2023, *msaexp: NIRSpec analysis tools*, [doi:10.5281/zenodo.8319596](#)
Brinchmann J., Charlot S., White S. D. M., Tremonti C., Kauffmann G., Heckman T., Brinkmann J., 2004, *MNRAS*, 351, 1151
Bruzual G., Charlot S., 2003, *MNRAS*, 344, 1000
Calzetti D., Armus L., Bohlin R. C., Kinney A. L., Koornneef J., Storchi-Bergmann T., 2000, *ApJ*, 533, 682
Carnall A. C., McLure R. J., Dunlop J. S., Dav e R., 2018, *MNRAS*, 480, 4379
Casey C. M., Narayanan D., Cooray A., 2014, *Phys. Rep.*, 541, 45
Chan S.-W., Ao Y., Tan Q., 2025, *arXiv e-prints*, p. [arXiv:2509.07913](#)
Chary R., Elbaz D., 2001, *ApJ*, 556, 562
Chen C.-C., et al., 2017, *ApJ*, 846, 108
Chiang I.-D., et al., 2024, *ApJ*, 964, 18
Civano F., et al., 2016, *VizieR Online Data Catalog: The COSMOS-Legacy Survey (CLS) catalog (Civano+, 2016), VizieR On-line Data Catalog: J/ApJ/819/62*. Originally published in: 2016ApJ...819...62C, [doi:10.26093/cds/vizieR.18190062](#)
Clements D. L., et al., 2008, *MNRAS*, 387, 247

- Cochrane R. K., Anglés-Alcázar D., Cullen F., Hayward C. C., 2024, *ApJ*, **961**, 37
- Cooper O. R., et al., 2025, *ApJ*, **982**, 125
- Coppin K. E. K., et al., 2012, *MNRAS*, **427**, 520
- Cowie L. L., Barger A. J., Kneib J.-P., 2002, *AJ*, **123**, 2197
- Cunha E., et al., 2015, *ApJ*, **806**, 110
- Curti M., Cresci G., Mannucci F., Marconi A., Maiolino R., Esposito S., 2017, *MNRAS*, **465**, 1384
- Curti M., Mannucci F., Cresci G., Maiolino R., 2020, *MNRAS*, **491**, 944
- Davies R. L., et al., 2021, *ApJ*, **909**, 78
- Decarli R., Díaz-Santos T., 2025, *A&A Rev.*, **33**, 4
- Donevski D., et al., 2020, *A&A*, **644**, A144
- Draine B. T., et al., 2007, *ApJ*, **663**, 866
- Dudzevičiūtė U., et al., 2020, *MNRAS*, **494**, 3828
- Dunlop J. S., et al., 2017, *MNRAS*, **466**, 861
- Dunlop J. S., et al., 2021, PRIMER: Public Release IMaging for Extragalactic Research, JWST Proposal. Cycle 1, ID. #1837
- Eisenstein D. J., et al., 2023, *arXiv e-prints*, p. [arXiv:2306.02465](https://arxiv.org/abs/2306.02465)
- Elbaz D., et al., 2011, *A&A*, **533**, A119
- Faisst A. L., et al., 2025, *ApJ*, **980**, 204
- Förster Schreiber N. M., Wuyts S., 2020, *ARA&A*, **58**, 661
- Fujimoto S., Ouchi M., Ono Y., Shibuya T., Ishigaki M., Nagai H., Momose R., 2016, *ApJS*, **222**, 1
- Fujimoto S., Ouchi M., Shibuya T., Nagai H., 2017, *ApJ*, **850**, 83
- Garg P., et al., 2022, *ApJ*, **926**, 80
- Genin A., et al., 2025, *A&A*, **699**, A343
- Giavalisco M., et al., 2004, *ApJ*, **600**, L93
- Gillman S., et al., 2021, *MNRAS*, **500**, 4229
- Gillman S., et al., 2022, *MNRAS*, **512**, 3480
- Gillman S., et al., 2023, *A&A*, **676**, A26
- Gillman S., et al., 2024, *A&A*, **691**, A299
- Gillman S., et al., 2025, *A&A*, **704**, A100
- Gómez-Guijarro C., et al., 2022, *A&A*, **659**, A196
- González Delgado R. M., Leitherer C., Heckman T. M., 1999, *ApJS*, **125**, 489
- Goto T., et al., 2003, *PASJ*, **55**, 771
- Greve T. R., et al., 2005, *MNRAS*, **359**, 1165
- Grogin N. A., et al., 2011, *ApJS*, **197**, 35
- Gullberg B., et al., 2019, *MNRAS*, **490**, 4956
- Gutkin J., Charlot S., Bruzual G., 2016, *MNRAS*, **462**, 1757
- Hamed M., Małek K., Buat V., Junais Ciesla L., Donevski D., Riccio G., Figueira M., 2023, *A&A*, **674**, A99
- Harikane Y., et al., 2025, *ApJ*, **993**, 204
- Hayward C. C., Narayanan D., Kereš D., Jonsson P., Hopkins P. F., Cox T. J., Hernquist L., 2013, *MNRAS*, **428**, 2529
- Head J. T. C. G., Lucey J. R., Hudson M. J., Smith R. J., 2014, *MNRAS*, **440**, 1690
- Heintz K. E., et al., 2025, *A&A*, **693**, A60
- Hickox R. C., Alexander D. M., 2018, *ARA&A*, **56**, 625
- Hirashita H., Ferrara A., Dayal P., Ouchi M., 2014, *MNRAS*, **443**, 1704
- Hirschmann M., Charlot S., Somerville R. S., 2023, *MNRAS*, **526**, 3504
- Hodge J. A., Carilli C. L., Walter F., de Blok W. J. G., Riechers D., Daddi E., Lentati L., 2012, *ApJ*, **760**, 11
- Hodge J. A., et al., 2013, *ApJ*, **768**, 91
- Hodge J. A., et al., 2025, *ApJ*, **978**, 165
- Hogan L., Rigopoulou D., Magdis G. E., Pereira-Santaella M., García-Bernete I., Thatte N., Grisdale K., Huang J. S., 2021, *MNRAS*, **503**, 5329
- Hunt L. K., et al., 2019, *A&A*, **621**, A51
- Ikarashi S., et al., 2015, *ApJ*, **810**, 133
- Ito K., et al., 2025, *arXiv e-prints*, p. [arXiv:2506.22642](https://arxiv.org/abs/2506.22642)
- Iverson R. J., Richard J., Biggs A. D., Zwaan M. A., Falgarone E., Arumugam V., van der Werf P. P., Rujopakarn W., 2020, *MNRAS*, **495**, L1
- Jakobsen P., et al., 2022, *A&A*, **661**, A80
- Jin S., et al., 2018, *ApJ*, **864**, 56
- Kaasinen M., Kewley L., Bian F., Groves B., Kashino D., Silverman J., Kartaltepe J., 2018, *MNRAS*, **477**, 5568
- Kashino D., Inoue A. K., 2019, *MNRAS*, **486**, 1053
- Kashino D., et al., 2017, *ApJ*, **835**, 88
- Kauffmann G., et al., 2003, *MNRAS*, **346**, 1055
- Kewley L. J., Dopita M. A., Sutherland R. S., Heisler C. A., Trevena J., 2001, *ApJ*, **556**, 121
- Kewley L. J., Maier C., Yabe K., Ohta K., Akiyama M., Dopita M. A., Yuan T., 2013, *ApJ*, **774**, L10
- Kewley L. J., Nicholls D. C., Sutherland R. S., 2019a, *ARA&A*, **57**, 511
- Kewley L. J., Nicholls D. C., Sutherland R., Rigby J. R., Acharya A., Dopita M. A., Bayliss M. B., 2019b, *ApJ*, **880**, 16
- Khostovan A. A., et al., 2025, *arXiv e-prints*, p. [arXiv:2512.16989](https://arxiv.org/abs/2512.16989)
- Kiyota T., et al., 2026, *arXiv e-prints*, p. [arXiv:2601.18149](https://arxiv.org/abs/2601.18149)
- Kocevski D. D., et al., 2018, *ApJS*, **236**, 48
- Kokorev V. I., et al., 2021, *ApJ*, **921**, 40
- Kriek M., Conroy C., 2013, *ApJ*, **775**, L16
- Kriek M., et al., 2015, *ApJS*, **218**, 15
- Kron R. G., 1980, *ApJS*, **43**, 305
- Kroupa P., 2002, *Science*, **295**, 82
- Lange R., et al., 2016, *MNRAS*, **462**, 1470
- Lawrence A., et al., 2007, *MNRAS*, **379**, 1599
- Lee M. M., et al., 2019, *ApJ*, **883**, L29
- Lee M. M., et al., 2025, *arXiv e-prints*, p. [arXiv:2511.20751](https://arxiv.org/abs/2511.20751)
- Lehmer B. D., Alexander D. M., Bauer F. E., Brandt W. N., Goulding A. D., Jenkins L. P., Ptak A., Roberts T. P., 2010, *ApJ*, **724**, 559
- Lelli F., Di Teodoro E. M., Fraternali F., Man A. W. S., Zhang Z.-Y., De Breuck C., Davis T. A., Maiolino R., 2021, *Science*, **371**, 713
- Leroy A. K., et al., 2011, *ApJ*, **737**, 12
- Leung G. C. K., et al., 2019, *ApJ*, **886**, 11
- Liao C.-L., et al., 2024, *ApJ*, **961**, 226
- Liu D., et al., 2019, *ApJS*, **244**, 40
- Long A. S., Casey C. M., del P. Lagos C., Lambrides E. L., Zavala J. A., Champagne J., Cooper O. R., Cooray A. R., 2023, *ApJ*, **953**, 11
- Lorenz B., et al., 2026, *arXiv e-prints*, p. [arXiv:2602.11418](https://arxiv.org/abs/2602.11418)
- Lovell C. C., Geach J. E., Davé R., Narayanan D., Coppin K. E. K., Li Q., Franco M., Privon G. C., 2022, *MNRAS*, **515**, 3644
- Lower S., Narayanan D., Li Q., Davé R., 2023, *ApJ*, **950**, 94
- Luo B., et al., 2017, VizieR Online Data Catalog: Chandra Deep Field-South survey: 7Ms sources (Luo+, 2017), VizieR On-line Data Catalog: J/ApJS/228/2. Originally published in: 2017ApJS...228....2L, doi:10.26093/cds/vizieer.22280002
- Lyu J., Alberts S., Rieke G. H., Rujopakarn W., 2022, *ApJ*, **941**, 191
- Lyu J., et al., 2024, *ApJ*, **966**, 229
- Madden S. C., et al., 2020, *A&A*, **643**, A141
- Magdis G. E., et al., 2012, *ApJ*, **760**, 6
- Magnelli B., et al., 2014, *A&A*, **561**, A86
- Magnelli B., et al., 2020, *ApJ*, **892**, 66
- Maiolino R., Mannucci F., 2019, *A&A Rev.*, **27**, 3
- Mannucci F., Cresci G., Maiolino R., Marconi A., Gnerucci A., 2010, *MNRAS*, **408**, 2115
- Martín N. S., et al., 2025, *ApJ*, **990**, 83
- McAlpine S., et al., 2019, *MNRAS*, **488**, 2440
- McKay S. J., Barger A. J., Cowie L. L., Nicandro Rosenthal M. J., 2025, *ApJ*, **988**, 135
- McKinney J., et al., 2024, *arXiv e-prints*, p. [arXiv:2408.08346](https://arxiv.org/abs/2408.08346)
- Menéndez-Delmestre K., Blain A. W., Swinbank M., Smail I., Iverson R. J., Chapman S. C., Gonçalves T. S., 2013, *ApJ*, **767**, 151
- Nakajima K., Ouchi M., 2014, *MNRAS*, **442**, 900
- Narayanan D., Krumholz M. R., Ostriker E. C., Hernquist L., 2012, *MNRAS*, **421**, 3127
- Nicandro Rosenthal M. J., McKay S. J., Barger A. J., Cowie L. L., 2026, *arXiv e-prints*, p. [arXiv:2601.20862](https://arxiv.org/abs/2601.20862)
- Oke J. B., Gunn J. E., 1983, *ApJ*, **266**, 713
- Osterbrock D. E., Ferland G. J., 2006, Astrophysics of gaseous nebulae and active galactic nuclei
- Padovani P., et al., 2017, *A&A Rev.*, **25**, 2
- Papovich C., et al., 2022, *ApJ*, **937**, 22
- Pasha I., Miller T. B., 2023, *The Journal of Open Source Software*, **8**, 5703
- Pearson W. J., et al., 2018, *A&A*, **615**, A146
- Pettini M., Pagel B. E. J., 2004, *MNRAS*, **348**, L59
- Polletta M., et al., 2024, *arXiv e-prints*, p. [arXiv:2405.07986](https://arxiv.org/abs/2405.07986)
- Pollock C. L., et al., 2025, *arXiv e-prints*, p. [arXiv:2506.15779](https://arxiv.org/abs/2506.15779)
- Poppo P., et al., 2023, *MNRAS*, **519**, 1526
- Popping G., Somerville R. S., Trager S. C., 2014, *MNRAS*, **442**, 2398
- Popping G., Somerville R. S., Galametz M., 2017, *MNRAS*, **471**, 3152
- Popping G., et al., 2022, *MNRAS*, **510**, 3321
- Price S. H., et al., 2025, *ApJ*, **982**, 51
- Puglisi A., et al., 2021, *MNRAS*, **508**, 5217
- Reddy N. A., et al., 2018, *ApJ*, **869**, 92
- Reddy N. A., et al., 2020, *ApJ*, **902**, 123
- Reddy N. A., Topping M. W., Sanders R. L., Shapley A. E., Brammer G., 2023, *ApJ*, **952**, 167
- Rémy-Ruyer A., et al., 2015, *A&A*, **582**, A121
- Ren J., et al., 2024, *arXiv e-prints*, p. [arXiv:2404.16686](https://arxiv.org/abs/2404.16686)
- Rigopoulou D., Pereira-Santaella M., Magdis G. E., Cooray A., Farrah D., Marques-Chaves R., Perez-Fournon I., Riechers D., 2018a, *MNRAS*, **473**, 20
- Rigopoulou D., Pereira-Santaella M., Magdis G. E., Cooray A., Farrah D., Marques-Chaves R., Perez-Fournon I., Riechers D., 2018b, *MNRAS*, **473**, 20
- Rizzo F., Vegetti S., Fraternali F., Stacey H. R., Powell D., 2021, *MNRAS*, **507**, 3952
- Sanders D. B., Soifer B. T., Elias J. H., Madore B. F., Matthews K., Neugebauer G., Scoville N. Z., 1988, *ApJ*, **325**, 74
- Sanders R. L., et al., 2016, *ApJ*, **816**, 23
- Sanders R. L., et al., 2021, *ApJ*, **914**, 19

- Schimiek A., Cicone C., Shen S., Decataldo D., Klaassen P., Mayer L., 2024, *A&A*, **687**, L10
- Schreiber C., et al., 2015, *A&A*, **575**, A74
- Scoville N., et al., 2007, *ApJS*, **172**, 1
- Shajib A. J., Treu T., Melo A., Roberts-Borsani G., Knabel S., Cappellari M., Frieman J. A., 2025, *A&A*, **702**, L12
- Shapley A. E., Cullen F., Dunlop J. S., McLure R. J., Kriek M., Reddy N. A., Sanders R. L., 2020, *ApJ*, **903**, L16
- Shapley A. E., Reddy N. A., Sanders R. L., Topping M. W., Brammer G. B., 2023, *ApJ*, **950**, L1
- Shapley A. E., et al., 2025, *ApJ*, **980**, 242
- Silverman J. D., et al., 2015, *ApJ*, **812**, L23
- Simpson J. M., et al., 2015, *ApJ*, **807**, 128
- Simpson J. M., et al., 2020, *MNRAS*, **495**, 3409
- Slob M., et al., 2024, *ApJ*, **973**, 131
- Speagle J. S., Steinhardt C. L., Capak P. L., Silverman J. D., 2014, *ApJS*, **214**, 15
- Stach S. M., et al., 2019, *MNRAS*, **487**, 4648
- Steidel C. C., et al., 2014, *ApJ*, **795**, 165
- Strom A. L., Steidel C. C., Rudie G. C., Trainor R. F., Pettini M., Reddy N. A., 2017, *ApJ*, **836**, 164
- Sun F., et al., 2026, *arXiv e-prints*, p. [arXiv:2601.15961](https://arxiv.org/abs/2601.15961)
- Suzuki T. L., et al., 2021, *ApJ*, **908**, 15
- Swinbank A. M., Smail I., Chapman S. C., Blain A. W., Ivison R. J., Keel W. C., 2004, *ApJ*, **617**, 64
- Swinbank A. M., et al., 2008, *MNRAS*, **391**, 420
- Swinbank A. M., et al., 2014, *MNRAS*, **438**, 1267
- Swinbank A. M., et al., 2019, *MNRAS*, **487**, 381
- Tacconi L. J., et al., 2013, *ApJ*, **768**, 74
- Tacconi L. J., et al., 2018, *ApJ*, **853**, 179
- Tadaki K.-i., et al., 2019, *ApJ*, **876**, 1
- Taylor et al., in prep., KAOSS Survey
- Topping M. W., et al., 2025, *MNRAS*, **541**, 1707
- Tremonti C. A., et al., 2004, *ApJ*, **613**, 898
- Usui M., et al., 2025, *ApJ*, **991**, L38
- Valentino F., et al., 2023, *ApJ*, **947**, 20
- Valentino F., et al., 2025, *arXiv e-prints*, p. [arXiv:2503.01990](https://arxiv.org/abs/2503.01990)
- Walter F., et al., 2016, *ApJ*, **833**, 67
- Ward B. A., Eales S. A., Ivison R. J., Arumugam V., 2024a, *MNRAS*, **530**, 4887
- Ward E., et al., 2024b, *ApJ*, **962**, 176
- Wardlow J. L., et al., 2017, *ApJ*, **837**, 12
- Wilson D., et al., 2017, *ApJ*, **848**, 30
- Wisnioski E., et al., 2018, *ApJ*, **855**, 97
- Witstok J., et al., 2022, *MNRAS*, **515**, 1751
- Zhang K., et al., 2017, *MNRAS*, **466**, 3217
- Zhang Z.-Y., et al., 2018, *MNRAS*, **481**, 59
- Zhang H., et al., 2019, *MNRAS*, **484**, 5170
- da Cunha E., Charlot S., Elbaz D., 2008, *MNRAS*, **388**, 1595
- de Graaff A., et al., 2025, *A&A*, **697**, A189
- ¹³ National Astronomical Observatory of Japan, 2-21-1 Osawa, Mitaka, Tokyo 181-8588, Japan
- ¹⁴ Department of Physics and Astronomy, School of Science, Kwansai Gakuin University, 1 Gakuen Uegahara, Sanda, Hyogo 669-1330, Japan
- ¹⁵ Astronomical Institute, Tohoku University, 6-3, Aramaki, Aoba, Sendai, Miyagi 980-8578, Japan
- ¹⁶ Subaru Telescope, National Astronomical Observatory of Japan, National Institutes of Natural Sciences (NINS), 650 North A'ohoku Place, Hilo, HI 96720, USA
- ¹⁷ Kapteyn Astronomical Institute, University of Groningen, Landleven 12, 9747 AD, Groningen, The Netherlands
- ¹⁸ MIT Kavli Institute for Astrophysics and Space Research, 70 Vassar Street, Cambridge, MA 02139, USA Graduate Institute of Astrophysics, National Taiwan University, Taipei 10617, Taiwan
- ¹⁹ Department of Physics and Center for Theoretical Physics, National Taiwan University, Taipei 10617, Taiwan

¹ Cosmic Dawn Center (DAWN), Denmark
e-mail: srigi@space.dtu.dk

² DTU-Space, Elektrovej, Building 328, 2800, Kgs. Lyngby, Denmark

³ Niels Bohr Institute, University of Copenhagen, Jagtvej 128, DK-2200, Copenhagen N, Denmark

⁴ Astronomy Centre, University of Sussex, Falmer, Brighton BN1 9QH, UK

⁵ Departamento de Física Teórica, Modulo 8, Facultad de Ciencias, Universidad Autónoma de Madrid, 28049 Madrid, Spain

⁶ CIAFF, Facultad de Ciencias, Universidad Autónoma de Madrid, 28049 Madrid, Spain

⁷ Affiliation: IPAC, California Institute of Technology, 1200 E. California Blvd. Pasadena, CA 91125, USA

⁸ David A. Dunlap Department of Astronomy and Astrophysics, University of Toronto, Toronto, ON M5S 3H4, Canada

⁹ Dunlap Institute for Astronomy and Astrophysics, University of Toronto, Toronto, ON M5S 3H4, Canada

¹⁰ Institute of Physics, Laboratory for galaxy evolution, Observatory of Sauverny, Chemin Pegasi 51, 1290 Versoix, Switzerland

¹¹ Department of Astrophysical Sciences, Princeton University, Princeton, NJ 08544, USA

¹² Department of Astronomical Science, The Graduate University for Advanced Studies, SOKENDAI, 2-21-1 Osawa, Mitaka, Tokyo 181-8588, Japan

Appendix A: Far-Infrared Selection

Table A.1: The source properties for the 48 far-infrared detected NIRSpec sources, ranked in descending infrared luminosity, as per Figure 1. For each source we list the NIRSpec ID (Column 1, C1), ALMA ID, either AS2UDS (A2-) or A3COSMOS (A3-) or ECOGAL (EG-) (C3), J2000 R.A. (C5), J2000 DEC. (C6), NIRSpec spectroscopic redshift (C7), ALMA primary beam corrected flux (C8), ALMA Band, ALMA – NIRSpec separation (C10). The NIRSpec ID is given as JWST program acronym (DD = DeepDive, RB = Rubies, JD = JADES, GR = George Rieke, GT = GTO, BA = BlueJay) followed by the DJA object-id (objid). DJA spectra file names are included in the online version of the table. Sources with no ALMA ID originate from the blind detection catalogue of the respective ALMA archival program. Sources identified as AGN (see Sec. 4.2) are highlighted, where † indicates broad emission lines, ‡ indicates an X-ray counterpart and * highlights elevated optical-line ratios.

NIRSpec ID	ALMA ID	R.A. [deg.]	Dec. [deg.]	z_{spec}	Flux [mJy]	Band	Sep ["]
RB-160718	A2-424.0	34.480165	-5.112523	3.5444	6.10±0.70	7	0.13
GT-167859	A3C-941026	150.163540	2.372423	2.0836	7.20±0.36	7	0.35
†‡*GR-172113	A3G-9834	53.148856	-27.821183	2.5829	4.22±0.12	7	0.01
‡JD-159764	A3G-15876	53.160581	-27.776188	2.5428	0.55±0.09	6	0.19
†DD-160970	A2-38.0	34.778015	-5.366046	2.5448	7.70±0.30	7	0.09
†BA-173854	A3C-892054	150.098507	2.365359	2.5554	0.42±0.12	4	0.09
‡JD-172437	A3G-16972	53.081969	-27.767276	2.3032	1.59±0.23	6	0.17
DD-147398	A3C-872955	149.908646	2.115584	2.9436	4.84±0.71	7	0.07
GR-172160	A3G-15639	53.181371	-27.777579	2.6974	4.94±0.84	8	0.02
GT-162506	A2-125.0	34.363199	-5.199367	2.1562	4.60±0.50	7	0.35
GT-162118	A2-272.0	34.461197	-5.201328	1.7059	5.10±0.50	7	0.05
JD-173408	A3G-3818	53.074866	-27.875907	4.4319	0.09±0.02	4	0.06
†‡*GR-172166	A3G-16274	53.131145	-27.773187	2.2245	0.04±0.01	4	0.02
†‡*JD-149659	A3G-10497	53.182003	-27.814182	2.6138	1.03±0.29	7	0.05
RB-151060	A2-346.0	34.273508	-5.251360	4.5440	3.60±0.30	7	0.13
JD-170092	A3G-54608	53.108837	-27.869126	3.7476	1.45±0.19	6	0.28
‡JD-167963	A3G-6131	53.091556	-27.853365	2.0346	2.76±0.50	7	0.29
RB-161829	A2-250.0	34.202863	-5.121150	3.9706	3.30±0.60	7	0.06
†‡JD-176494	A3G-15432	53.146178	-27.779934	2.5834	0.23±0.06	6	0.03
GT-169541	A3C-893896	150.130915	2.208874	2.3032	0.11±0.03	4	0.27
‡JD-164819	A3G-	53.091784	-27.712084	1.6153	2.86±0.54	7	0.35
†GR-175918	A3G-20173	53.154439	-27.738678	2.3279	0.81±0.25	6	0.06
RB-163266	A2-427.0	34.301094	-5.287985	4.8041	2.40±0.50	7	0.08
†‡GT-162424	EG-127505	34.337315	-5.143674	4.5560	2.37±0.29	7	0.03
BA-155180	A3C-	150.112224	2.313952	2.0977	1.08±0.21	6	0.45
GR-172171	A3G-45150	53.137103	-27.761408	1.8130	0.84±0.04	6	0.08
RB-157952	EG-138976	34.276132	-5.163512	5.2172	0.24±0.05	4	0.30
JD-175480	A3G-22281	53.097333	-27.720451	2.5651	1.82±0.22	7	0.12
†BA-173819	A3C-765691	150.086472	2.264299	2.4934	0.14±0.04	6	0.13
DD-150418	A2-659.0	34.445445	-5.130508	1.8187	1.70±0.30	7	0.08
‡JD-163721	A3G-7551	53.131446	-27.841383	1.6145	0.43±0.03	4	0.03
GT-169474	A3C-481073	150.166891	2.235805	1.8404	0.42±0.09	6	0.04
BA-173884	A3C-320337	150.087998	2.395073	3.5328	1.34±0.16	7	0.14
DD-149715	A3C-77714	150.077170	2.380370	2.8107	0.44±0.03	6	0.05
GT-173952	A2-2.0	34.465044	-5.251940	2.3039	1.02±0.18	7	0.27
‡GT-175747	EG-133443	34.415788	-5.171871	1.9168	1.04±0.15	7	0.04
‡GR-172157	A3G-15381	53.180521	-27.779717	2.6935	0.36±0.10	6	0.03
GT-162594	EG-129470	34.471635	-5.256968	2.5264	0.96±0.16	7	0.05
GR-175915	A3G-20740	53.171807	-27.733608	2.5750	0.06±0.01	4	0.25
EX-172449	EG-82011	34.350624	-5.149878	4.6229	0.77±0.08	7	0.06
GR-146584	A3G-15336	53.179110	-27.780619	1.0372	0.17±0.04	6	0.02
‡JD-172117	A3G-10832	53.161428	-27.811149	2.8233	0.39±0.12	6	0.06
JD-176095	A3G-22642	53.052276	-27.718373	1.8070	3.12±0.85	9	0.11
GR-172150	A3G-14638	53.176590	-27.785521	1.3172	0.19±0.06	6	0.06
GR-172162	A3G-15844	53.170916	-27.775426	2.4542	0.15±0.03	6	0.03
‡JD-146516	A3G-	53.155657	-27.779365	1.8469	0.12±0.02	6	0.18
GR-172152	A3G-15016	53.173693	-27.782134	1.9981	0.10±0.02	6	0.07
JD-172382	A3G-15927	53.095744	-27.774815	4.4374	0.26±0.07	7	0.17

Appendix B: Emission-Line Properties

Table B.1: Observed (dust un-corrected) emission line properties for the 48 far-infrared detected NIRSspec sources, ranked in descending infrared luminosity, as per Figure 1. For each source we list the NIRSspec ID (Column 1, C1), NIRSspec spectroscopic redshift (C2), Balmer decrement (C3), [OIII]/H β ratio (C5), [NII]/H α ratio (C6), [NII]/H α derived gas-phase metallicity (C7), [SII] doublet ratio (C8), [SII] derived electron density (C9). For low signal to noise emission lines detected we define a 3σ limit in the respective calculation, as indicated by the inequalities. Sources identified as AGN (see Sec. 4.2) are highlighted, where † indicates broad emission lines, ‡ indicates an X-ray counterpart and * highlights elevated optical-line ratios.

NIRSspec ID	z_{spec}	$\frac{\text{H}\alpha}{\text{H}\beta}$	$A_{\text{V,Balmer}}$	$\frac{[\text{OIII } 5007\lambda]}{\text{H}\beta}$	$\frac{[\text{NII}]}{\text{H}\alpha}$	$12+\log(\text{O}/\text{H})$	$\frac{[\text{SII } 6716\lambda]}{[\text{SII } 6731\lambda]}$	$\log_{10}(n_e)$ [cm $^{-3}$]
RB-160718	3.5444	-	-	-	0.55±0.15	8.69±0.06	-	-
GT-167859	2.0836	-	-	-	0.36±0.08	8.61±0.05	-	-
†*GR-172113	2.5829	>2.73	-	>40.95	<1.36	<8.89	-	-
‡JD-159764	2.5428	3.85±0.26	1.11±0.23	1.43±0.10	0.27±0.02	8.54±0.02	1.05±0.14	2.40±0.30
†DD-160970	2.5448	>2.36	-	-	0.81±0.19	8.77±0.05	-	-
†BA-173854	2.5554	>1.78	-	-	<1.31	<8.92	-	-
‡JD-172437	2.3032	-	-	-	0.75±0.11	8.76±0.03	<1.09	>2.33
DD-147398	2.9436	>0.93	-	>1.71	<0.54	<8.69	-	-
GR-172160	2.6974	>0.43	-	-	0.59±0.16	8.71±0.06	-	-
GT-162506	2.1562	-	-	-	0.82±0.12	8.78±0.03	-	-
GT-162118	1.7059	-	-	-	0.84±0.31	8.78±0.08	-	-
JD-173408	4.4319	-	-	-	0.56±0.08	8.70±0.03	-	-
†*GR-172166	2.2245	12.44±5.66	5.17±1.18	7.15±2.85	1.34±0.57	8.88±0.09	-	-
†*JD-149659	2.6138	>3.54	-	>0.78	0.86±0.15	8.79±0.04	<0.76	>2.89
RB-151060	4.5440	-	-	-	0.72±0.19	8.75±0.06	-	-
JD-170092	3.7476	>2.72	-	-	0.60±0.15	8.71±0.05	-	-
‡JD-167963	2.0346	-	-	-	0.52±0.10	8.68±0.04	-	-
RB-161829	3.9706	-	-	-	1.01±0.20	8.82±0.04	-	-
†‡JD-176494	2.5834	-	-	-	1.25±0.20	8.87±0.03	<0.69	>3.04
GT-169541	2.3032	-	-	-	<0.71	<8.75	-	-
‡JD-164819	1.6153	3.92±1.73	1.19±0.97	0.82±0.50	0.37±0.06	8.61±0.04	-	-
†GR-175918	2.3279	-	-	-	0.95±0.08	8.81±0.02	0.89±0.00	2.66±0.00
RB-163266	4.8041	-	-	-	1.74±0.68	8.94±0.08	-	-
†‡GT-162424	4.5560	-	-	-	<0.71	<8.75	-	-
BA-155180	2.0977	6.40±0.58	2.86±0.32	0.39±0.07	0.33±0.03	8.59±0.02	<0.98	>2.50
GR-172171	1.8130	>2.88	-	-	0.62±0.12	8.72±0.04	-	-
RB-157952	5.2172	>4.85	-	>1.31	0.42±0.04	8.63±0.02	<0.92	>2.59
JD-175480	2.5651	>1.45	-	-	0.57±0.12	8.70±0.05	-	-
†BA-173819	2.4934	6.00±0.59	2.66±0.34	-	0.18±0.04	8.46±0.05	<0.58	>3.35
DD-150418	1.8187	-	-	-	0.69±0.11	8.74±0.03	-	-
‡JD-163721	1.6145	-	-	-	1.35±0.19	8.88±0.03	-	-
GT-169474	1.8404	-	-	-	0.46±0.07	8.65±0.03	-	-
BA-173884	3.5328	6.89±0.63	3.13±0.31	1.81±0.19	0.34±0.02	8.59±0.01	0.90±0.18	2.63±0.44
DD-149715	2.8107	7.22±0.59	3.30±0.28	1.28±0.13	0.43±0.02	8.64±0.01	1.04±0.09	2.41±0.16
GT-173952	2.3039	-	-	-	0.24±0.04	8.52±0.03	-	-
‡GT-175747	1.9168	-	-	-	1.23±0.39	8.86±0.07	-	-
‡GR-172157	2.6935	5.68±5.56	2.43±1.18	1.05±1.24	0.53±0.07	8.69±0.03	<1.67	>0.07
GT-162594	2.5264	>0.89	-	-	0.63±0.14	8.72±0.05	-	-
GR-175915	2.5750	-	-	-	1.10±0.13	8.84±0.02	-	-
EX-172449	4.6229	2.55±0.13	-0.30±0.17	3.32±0.17	0.19±0.01	8.46±0.01	1.06±0.26	2.37±0.82
GR-146584	1.0372	18.10±8.50	6.46±1.05	-	0.49±0.02	8.67±0.01	0.77±0.11	2.89±0.26
‡JD-172117	2.8233	-	-	-	0.79±0.09	8.77±0.02	<1.51	>0.07
JD-176095	1.8070	-	-	-	0.46±0.16	8.66±0.08	-	-
GR-172150	1.3172	-	-	-	1.22±0.09	8.86±0.02	<0.92	>2.59
GR-172162	2.4542	5.13±2.06	2.14±0.98	1.06±6.32	0.49±0.06	8.67±0.03	<1.27	>1.90
‡JD-146516	1.8469	5.03±0.81	2.04±0.53	0.88±0.20	0.40±0.04	8.63±0.02	0.95±0.17	2.56±0.38
GR-172152	1.9981	>2.93	-	-	0.79±0.13	8.77±0.03	-	-
JD-172382	4.4374	-	-	-	0.13±0.01	8.39±0.01	1.02±0.14	2.43±0.27

Appendix C: SED Modelling

Table C.1: The SED properties for the 48 far-infrared detected NIRSspec sources, ranked in descending infrared luminosity, as per Figure 1. For each source we list the DeepDive ID (Column 1, C1), NIRSspec spectroscopic redshift (C2), bagpipes derived stellar mass (C3), star-formation rate (C4) and dust attenuation (C5). We further list the mercurius derived dust mass (C6), far-infrared luminosity (C7), dust temperature (C8), as well as the PySersic derived $0.5\mu\text{m}$ effective radius (C9) and Sérsic index (C10). Sources identified as AGN (see Sec. 4.2) are highlighted, where † indicates broad emission lines, ‡ indicates an X-ray counterpart and * highlights elevated optical-line ratios.

ID	z_{spec}	$\log_{10}(M_*)$ [M_{\odot}]	SFR [$M_{\odot} \text{ yr}^{-1}$]	A_V [mag]	$\log_{10}(M_d)$ [M_{\odot}]	L_{FIR} [L_{\odot}]	T_d [K]	$R_{e,0.5\mu\text{m}}$ [kpc]	$n_{0.5\mu\text{m}}$
RB-160718	3.5444	10.69±0.08	67.04±41.81	2.76±0.46	9.06 ^{+0.08} _{-0.09}	12.69 ^{+0.05} _{-0.06}	37.37 ^{+1.79} _{-1.74}	1.36 ^{+0.21} _{-0.21}	0.67 ^{+0.04} _{-0.02}
GT-167859	2.0836	10.98±0.04	64.51±23.53	0.70±0.14	9.18 ^{+0.03} _{-0.03}	12.63 ^{+0.01} _{-0.02}	34.67 ^{+0.58} _{-0.56}	4.04 ^{+0.04} _{-0.04}	0.93 ^{+0.03} _{-0.03}
†‡*GR-172113	2.5829	11.10±0.03	21.76±5.35	0.56±0.15	8.90 ^{+0.02} _{-0.02}	12.61 ^{+0.01} _{-0.01}	38.64 ^{+0.31} _{-0.32}	2.74 ^{+0.01} _{-0.01}	0.94 ^{+0.01} _{-0.01}
‡JD-159764	2.5428	10.46±0.03	30.48±3.75	0.72±0.07	8.40 ^{+0.09} _{-0.12}	12.57 ^{+0.03} _{-0.04}	47.16 ^{+2.03} _{-1.58}	2.46 ^{+0.06} _{-0.06}	0.65 ^{+0.00} _{-0.00}
†DD-160970	2.5448	11.14±0.10	112.85±60.00	3.01±0.48	9.40 ^{+0.04} _{-0.04}	12.48 ^{+0.05} _{-0.06}	30.24 ^{+1.01} _{-1.01}	5.25 ^{+0.29} _{-0.25}	1.12 ^{+0.09} _{-0.09}
†BA-173854	2.5554	11.41±0.06	189.09±108.81	3.09±0.63	9.43 ^{+0.05} _{-0.05}	12.47 ^{+0.02} _{-0.02}	29.79 ^{+0.70} _{-0.68}	3.51 ^{+0.13} _{-0.12}	1.92 ^{+0.09} _{-0.08}
‡JD-172437	2.3032	11.41±0.07	98.05±47.01	3.81±0.23	8.89 ^{+0.05} _{-0.06}	12.41 ^{+0.02} _{-0.02}	35.62 ^{+1.33} _{-0.60}	-	-
DD-147398	2.9436	11.29±0.09	0.13±103.03	2.31±0.77	9.18 ^{+0.08} _{-0.08}	12.40 ^{+0.05} _{-0.05}	31.92 ^{+1.24} _{-1.20}	-	-
GR-172160	2.6974	10.90±0.03	60.36±11.93	2.53±0.17	8.84 ^{+0.10} _{-0.12}	12.36 ^{+0.04} _{-0.05}	35.72 ^{+1.02} _{-1.31}	3.61 ^{+0.05} _{-0.05}	0.92 ^{+0.03} _{-0.03}
GT-162506	2.1562	11.49±0.07	303.11±90.16	2.10±0.14	9.17 ^{+0.07} _{-0.07}	12.35 ^{+0.06} _{-0.06}	31.36 ^{+1.27} _{-1.27}	5.53 ^{+0.27} _{-0.23}	0.86 ^{+0.08} _{-0.07}
GT-162118	1.7059	11.06±0.07	76.95±28.09	2.71±0.24	9.24 ^{+0.06} _{-0.06}	12.33 ^{+0.04} _{-0.05}	30.36 ^{+1.03} _{-0.99}	3.98 ^{+0.04} _{-0.04}	0.87 ^{+0.02} _{-0.02}
JD-173408	4.4319	10.69±0.03	56.19±8.01	1.68±0.08	9.14 ^{+0.09} _{-0.12}	12.20 ^{+0.09} _{-0.12}	30	1.99 ^{+0.02} _{-0.02}	0.93 ^{+0.03} _{-0.03}
†‡*GR-172166	2.2245	10.91±0.04	263.68±41.87	1.44±0.06	8.62 ^{+0.09} _{-0.10}	12.20 ^{+0.03} _{-0.03}	36.57 ^{+1.25} _{-1.02}	2.09 ^{+0.01} _{-0.01}	3.99 ^{+0.03} _{-0.03}
†‡*JD-149659	2.6138	10.50±0.05	3.81±6.07	1.56±0.45	7.75 ^{+0.18} _{-0.23}	12.19 ^{+0.05} _{-0.06}	53.72 ^{+5.48} _{-3.67}	1.42 ^{+0.01} _{-0.01}	0.66 ^{+0.01} _{-0.01}
RB-151060	4.5440	10.66±0.08	64.71±27.40	3.36±0.35	9.09 ^{+0.04} _{-0.04}	12.15 ^{+0.04} _{-0.04}	30	2.02 ^{+0.33} _{-0.26}	1.01 ^{+0.31} _{-0.24}
JD-170092	3.7476	10.83±0.06	55.68±36.42	3.61±0.60	9.05 ^{+0.06} _{-0.06}	12.11 ^{+0.06} _{-0.06}	30	12.14 ^{+3.14} _{-2.75}	1.61 ^{+0.46} _{-0.38}
‡JD-167963	2.0346	11.16±0.03	64.30±9.91	3.94±0.08	8.74 ^{+0.10} _{-0.11}	12.09 ^{+0.03} _{-0.03}	33.45 ^{+1.20} _{-1.08}	2.48 ^{+0.01} _{-0.01}	1.02 ^{+0.01} _{-0.01}
RB-161829	3.9706	10.79±0.08	141.57±80.83	2.16±0.22	9.02 ^{+0.08} _{-0.09}	12.08 ^{+0.08} _{-0.09}	30	2.31 ^{+0.06} _{-0.06}	0.78 ^{+0.06} _{-0.07}
†‡JD-176494	2.5834	10.71±0.04	11.48±5.64	1.11±0.19	7.74 ^{+0.26} _{-0.29}	12.07 ^{+0.21} _{-0.37}	51.18 ^{+13.40} _{-11.81}	1.19 ^{+0.01} _{-0.01}	1.40 ^{+0.03} _{-0.04}
GT-169541	2.3032	10.96±0.06	56.71±17.71	3.76±0.33	8.39 ^{+0.14} _{-0.15}	12.07 ^{+0.05} _{-0.05}	38.08 ^{+2.70} _{-2.35}	4.41 ^{+0.50} _{-0.40}	2.99 ^{+0.31} _{-0.29}
‡JD-164819	1.6153	10.58±0.08	12.28±19.48	1.15±0.46	8.88 ^{+0.09} _{-0.11}	12.03 ^{+0.02} _{-0.02}	31.09 ^{+1.11} _{-0.92}	-	-
†GR-175918	2.3279	10.72±0.06	0.00±6.29	1.16±0.36	8.41 ^{+0.19} _{-0.24}	12.00 ^{+0.06} _{-0.07}	36.66 ^{+2.91} _{-1.94}	1.76 ^{+0.04} _{-0.04}	3.78 ^{+0.11} _{-0.10}
RB-163266	4.8041	10.73±0.08	93.63±41.58	2.34±0.24	8.91 ^{+0.10} _{-0.12}	11.96 ^{+0.10} _{-0.12}	30	1.62 ^{+0.99} _{-0.43}	3.40 ^{+1.82} _{-1.13}
†‡GT-162424	4.5560	11.47±0.01	0.00±0.10	0.01±0.01	8.91 ^{+0.05} _{-0.06}	11.96 ^{+0.05} _{-0.06}	30	0.14 ^{+0.01} _{-0.01}	1.59 ^{+1.12} _{-0.90}
BA-155180	2.0977	11.08±0.07	85.73±33.11	2.97±0.23	8.88 ^{+0.08} _{-0.10}	11.93 ^{+0.08} _{-0.10}	30	4.31 ^{+0.08} _{-0.09}	0.72 ^{+0.03} _{-0.03}
GR-172171	1.8130	10.67±0.04	3.83±16.31	2.15±0.33	8.85 ^{+0.02} _{-0.02}	11.91 ^{+0.02} _{-0.02}	30	5.80 ^{+0.03} _{-0.03}	0.83 ^{+0.01} _{-0.01}
RB-157952	5.2172	10.81±0.12	190.14±66.97	2.97±0.24	8.83 ^{+0.08} _{-0.09}	11.89 ^{+0.08} _{-0.09}	30	3.37 ^{+0.64} _{-0.47}	2.11 ^{+0.53} _{-0.42}
JD-175480	2.5651	10.57±0.06	30.04±10.77	2.25±0.29	8.78 ^{+0.05} _{-0.06}	11.83 ^{+0.05} _{-0.06}	30	-	-
†BA-173819	2.4934	10.34±0.03	15.74±1.43	0.17±0.09	6.90 ^{+0.60} _{-0.53}	11.83 ^{+0.10} _{-0.16}	71.86 ^{+29.42} _{-21.23}	3.25 ^{+0.13} _{-0.13}	2.13 ^{+0.17} _{-0.17}
DD-150418	1.8187	11.34±0.07	108.56±54.74	3.40±0.35	8.75 ^{+0.08} _{-0.09}	11.81 ^{+0.08} _{-0.09}	30	4.28 ^{+0.05} _{-0.06}	0.71 ^{+0.03} _{-0.03}
‡JD-163721	1.6145	11.26±0.06	46.72±22.89	2.50±0.28	9.35 ^{+0.09} _{-0.10}	11.81 ^{+0.03} _{-0.03}	24.49 ^{+0.76} _{-0.64}	4.90 ^{+0.02} _{-0.02}	2.20 ^{+0.02} _{-0.02}
GT-169474	1.8404	11.14±0.08	123.55±62.95	3.13±0.23	8.42 ^{+0.66} _{-0.34}	11.71 ^{+0.15} _{-1.36}	33.26 ^{+5.57} _{-16.00}	3.11 ^{+0.03} _{-0.03}	0.95 ^{+0.02} _{-0.02}
BA-173884	3.5328	10.71±0.08	152.29±45.56	1.73±0.14	8.64 ^{+0.05} _{-0.06}	11.70 ^{+0.05} _{-0.06}	30	2.49 ^{+0.08} _{-0.07}	1.12 ^{+0.08} _{-0.07}
DD-149715	2.8107	10.89±0.08	143.63±44.18	1.99±0.17	8.64 ^{+0.03} _{-0.03}	11.69 ^{+0.03} _{-0.03}	30	2.81 ^{+0.08} _{-0.08}	1.39 ^{+0.08} _{-0.09}
GT-173952	2.3039	10.94±0.06	67.59±24.51	3.10±0.27	8.63 ^{+0.05} _{-0.06}	11.69 ^{+0.05} _{-0.06}	30	4.44 ^{+0.37} _{-0.28}	1.56 ^{+0.18} _{-0.15}
‡GT-175747	1.9168	10.98±0.06	59.11±18.72	2.72±0.20	8.54 ^{+0.06} _{-0.07}	11.59 ^{+0.06} _{-0.07}	30	2.59 ^{+0.04} _{-0.04}	0.94 ^{+0.05} _{-0.05}
‡GR-172157	2.6935	10.73±0.04	43.55±9.00	2.20±0.10	8.51 ^{+0.12} _{-0.17}	11.56 ^{+0.12} _{-0.17}	30	4.99 ^{+0.10} _{-0.09}	1.78 ^{+0.04} _{-0.04}
GT-162594	2.5264	10.60±0.07	39.12±18.91	2.11±0.33	8.49 ^{+0.07} _{-0.09}	11.55 ^{+0.07} _{-0.09}	30	3.34 ^{+0.16} _{-0.14}	0.72 ^{+0.06} _{-0.05}
GR-175915	2.5750	10.08±0.05	0.01±1.33	1.05±0.44	8.45 ^{+0.10} _{-0.13}	11.51 ^{+0.10} _{-0.13}	30	1.65 ^{+0.04} _{-0.04}	0.70 ^{+0.05} _{-0.03}
EX-172449	4.6229	9.96±0.08	29.04±6.76	0.48±0.11	8.42 ^{+0.04} _{-0.04}	11.47 ^{+0.04} _{-0.04}	30	1.36 ^{+0.04} _{-0.04}	1.57 ^{+0.11} _{-0.12}
GR-146584	1.0372	10.78±0.06	0.43±1.76	2.26±0.48	8.07 ^{+0.05} _{-0.05}	11.47 ^{+0.01} _{-0.01}	34.09 ^{+0.60} _{-0.61}	2.06 ^{+0.01} _{-0.01}	1.04 ^{+0.01} _{-0.01}
‡JD-172117	2.8233	10.99±0.04	0.00±0.20	2.32±0.36	8.35 ^{+0.16} _{-0.31}	11.41 ^{+0.16} _{-0.31}	30	2.18 ^{+0.03} _{-0.03}	2.24 ^{+0.09} _{-0.07}
JD-176095	1.8070	10.51±0.07	15.82±9.85	1.42±0.31	8.30 ^{+0.12} _{-0.17}	11.36 ^{+0.12} _{-0.17}	30	-	-
GR-172150	1.3172	10.89±0.07	18.54±10.84	2.37±0.34	7.66 ^{+0.18} _{-0.17}	11.29 ^{+0.05} _{-0.05}	37.35 ^{+2.23} _{-2.15}	3.23 ^{+0.01} _{-0.01}	2.48 ^{+0.03} _{-0.03}
GR-172162	2.4542	10.51±0.07	39.34±13.87	2.41±0.20	8.07 ^{+0.07} _{-0.09}	11.12 ^{+0.07} _{-0.09}	30	2.64 ^{+0.05} _{-0.05}	1.14 ^{+0.03} _{-0.03}
‡JD-146516	1.8469	10.39±0.03	104.24±37.03	1.44±0.07	8.06 ^{+0.07} _{-0.09}	11.11 ^{+0.07} _{-0.09}	30	4.08 ^{+0.01} _{-0.01}	0.92 ^{+0.01} _{-0.01}
GR-172152	1.9981	10.24±0.06	0.65±1.93	1.68±0.27	7.99 ^{+0.08} _{-0.11}	11.05 ^{+0.08} _{-0.11}	30	2.14 ^{+0.01} _{-0.01}	1.24 ^{+0.02} _{-0.02}
JD-172382	4.4374	9.68±0.09	57.26±12.73	1.06±0.05	7.89 ^{+0.13} _{-0.20}	10.94 ^{+0.13} _{-0.20}	30	1.63 ^{+0.04} _{-0.04}	0.90 ^{+0.05} _{-0.06}

Appendix D: NIRSspec Spectra

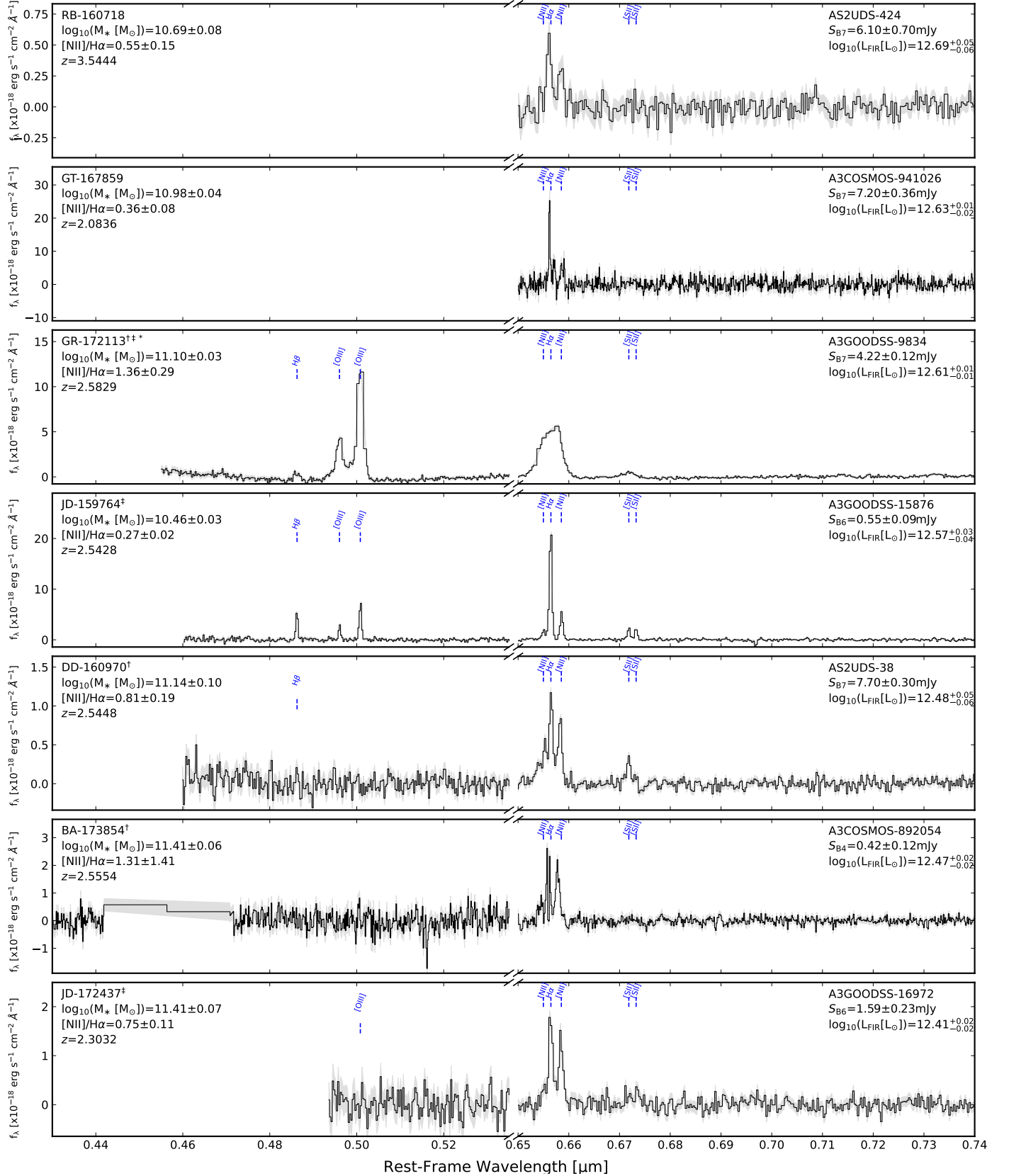


Fig. D.1: JWST/NIRSspec spectra for the 48 far-infrared detected NIRSspec sources, ranked in descending far-infrared luminosity. For each source we show the NIRSspec spectra (and 1σ uncertainty) from rest-frame 0.46–0.54 μm highlighting the [OIII]/H β complex and 0.65–0.74 μm highlighting the [NII]/H α complex, with detected ($>3\sigma$) emission lines labelled. We further indicate the NIRSspec ID, bagpipes derived stellar mass, [NII]/H α index, spectroscopic redshift as well as ALMA ID, ALMA selection band, flux density and mercurius far-infrared luminosity of each source. The grey shaded region indicates the NIRSspec detector gap.

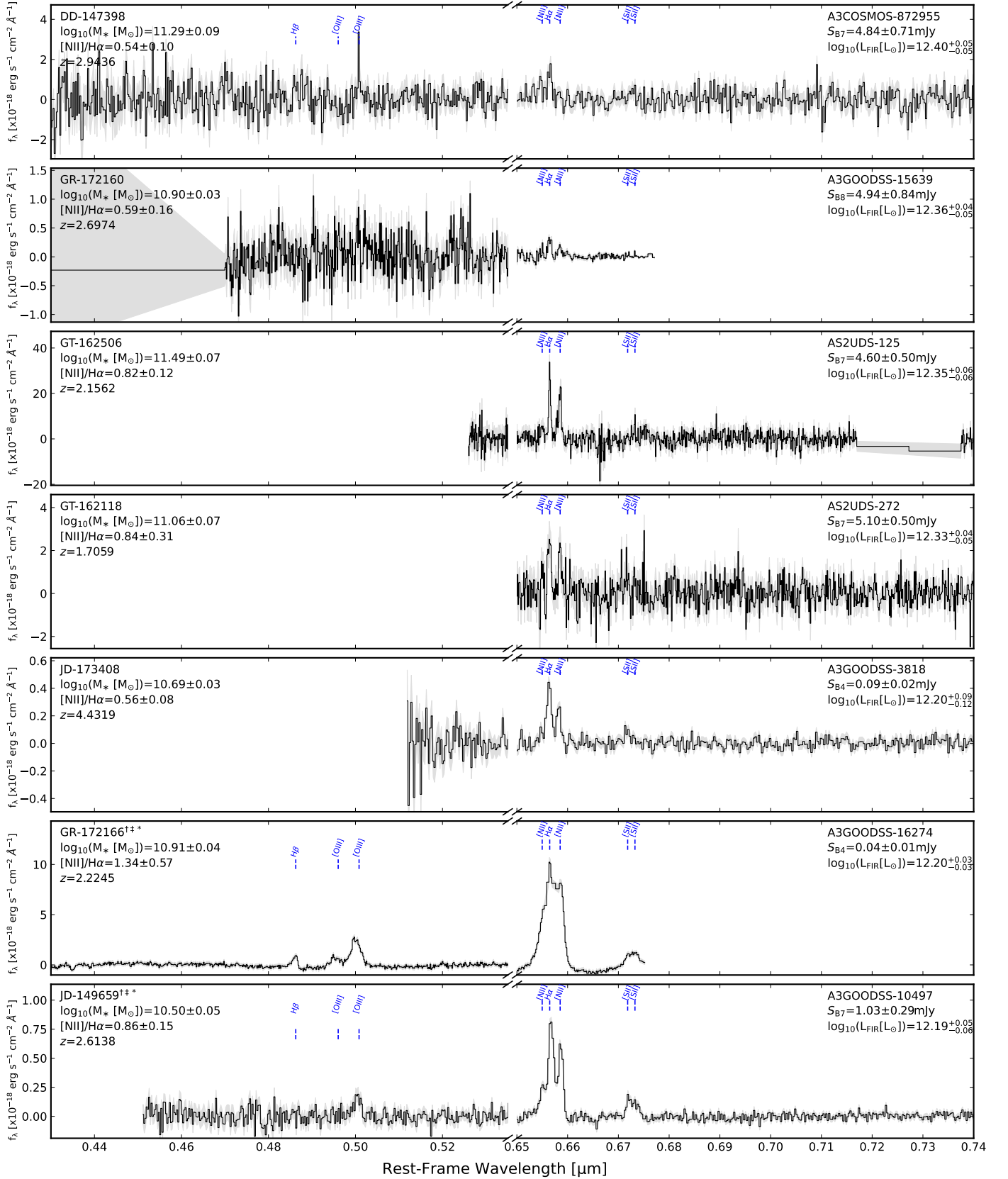


Fig. D.2: Continued...

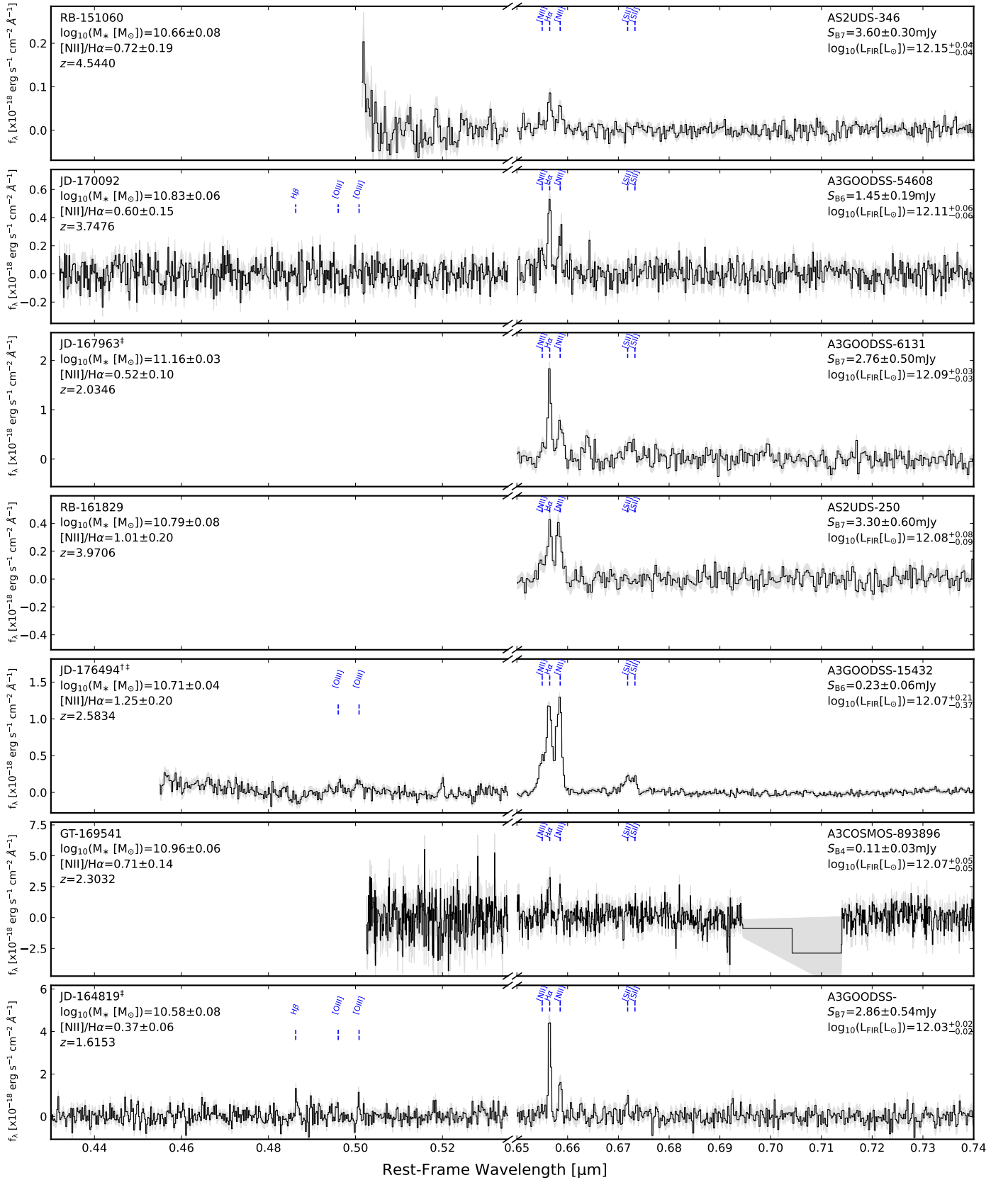


Fig. D.3: Continued...

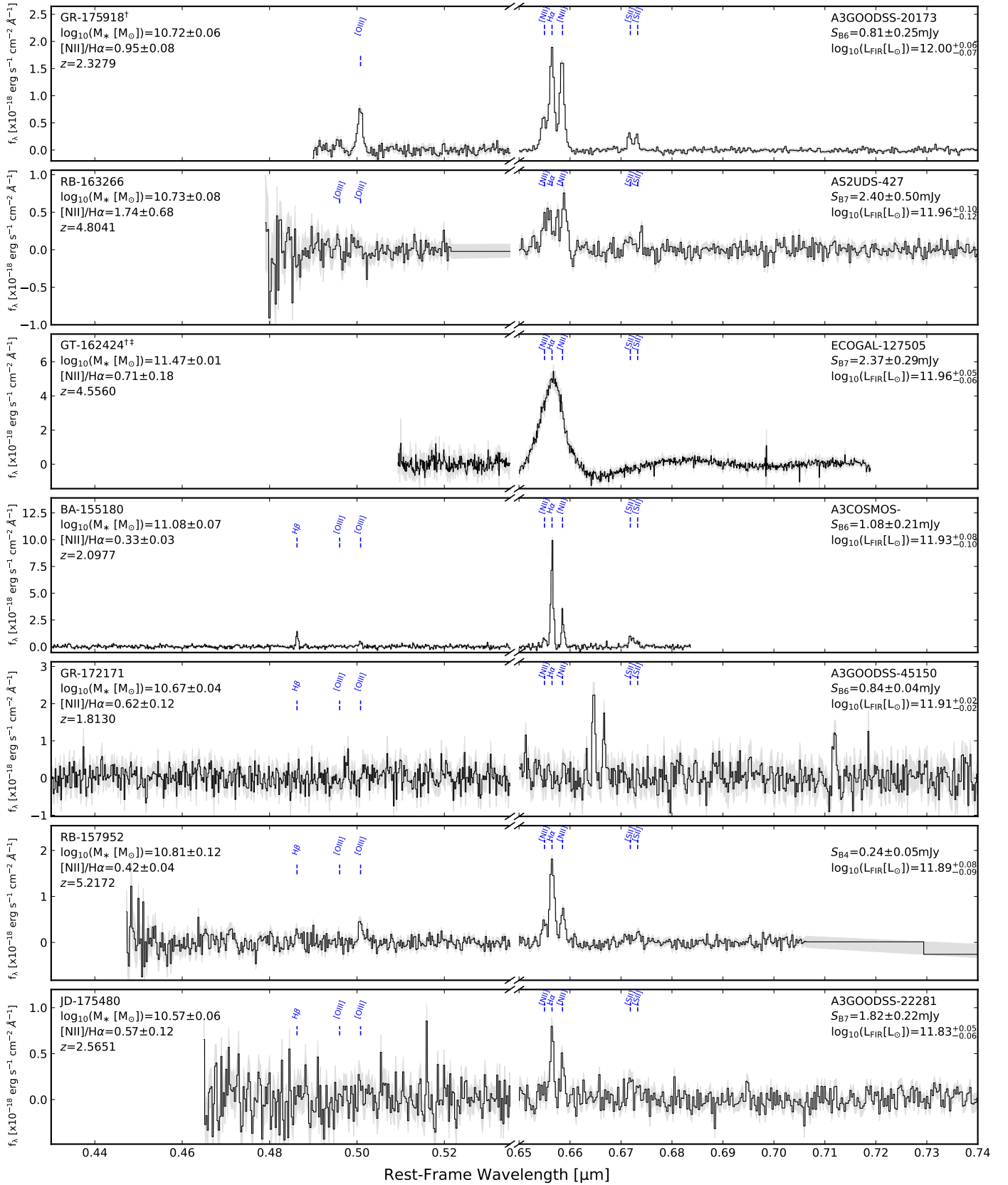


Fig. D.4: Continued...

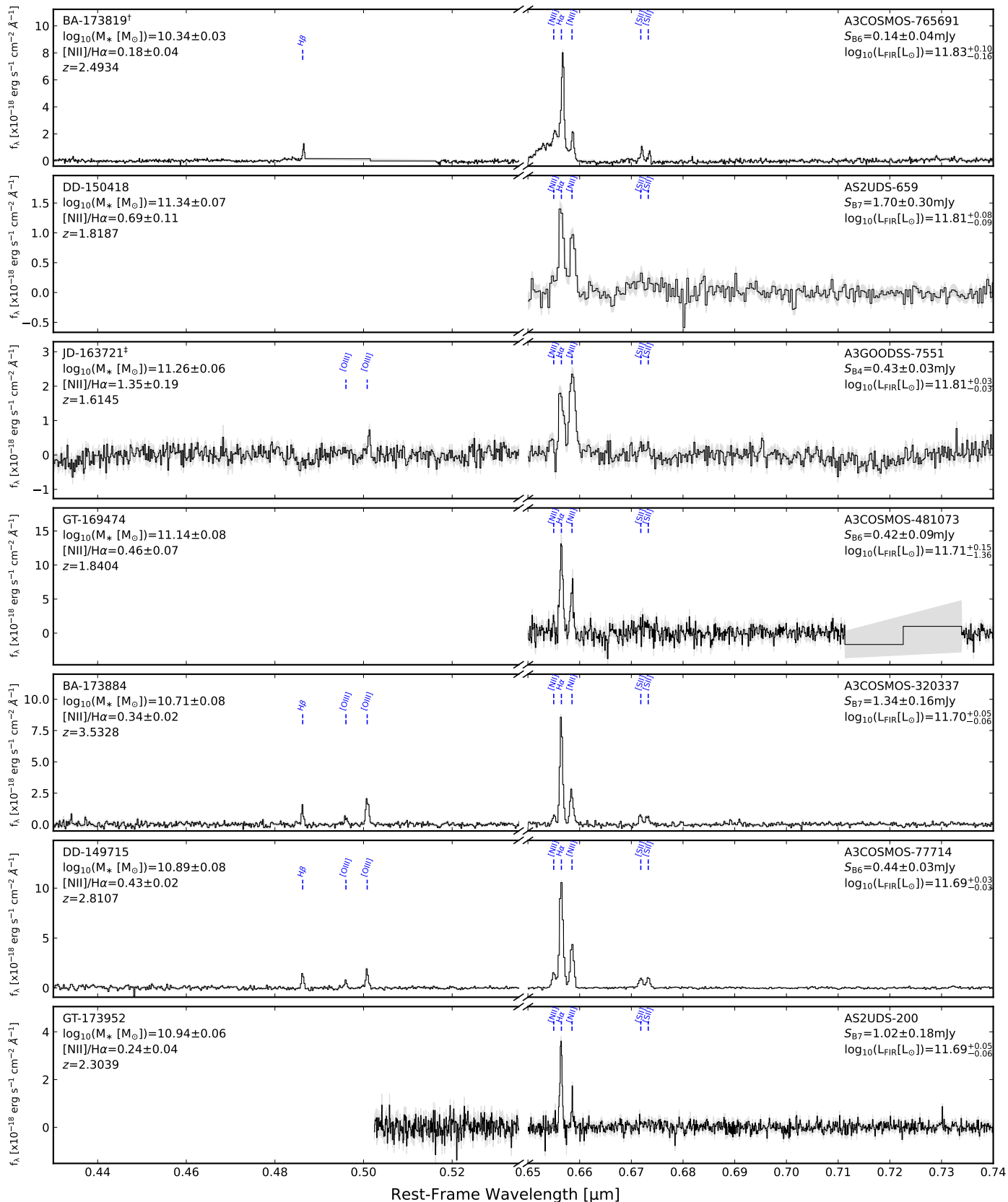


Fig. D.5: Continued...

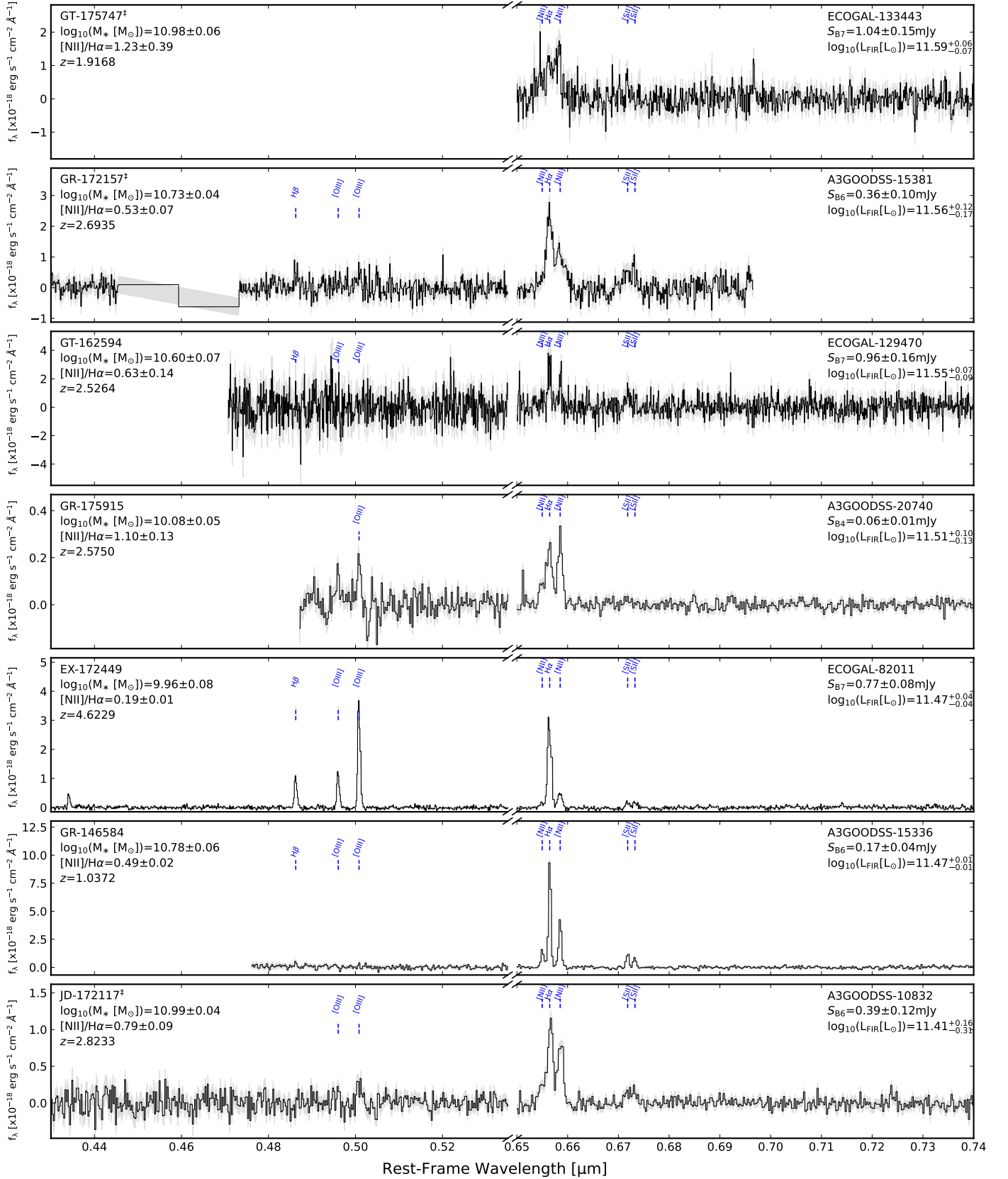


Fig. D.6: Continued...

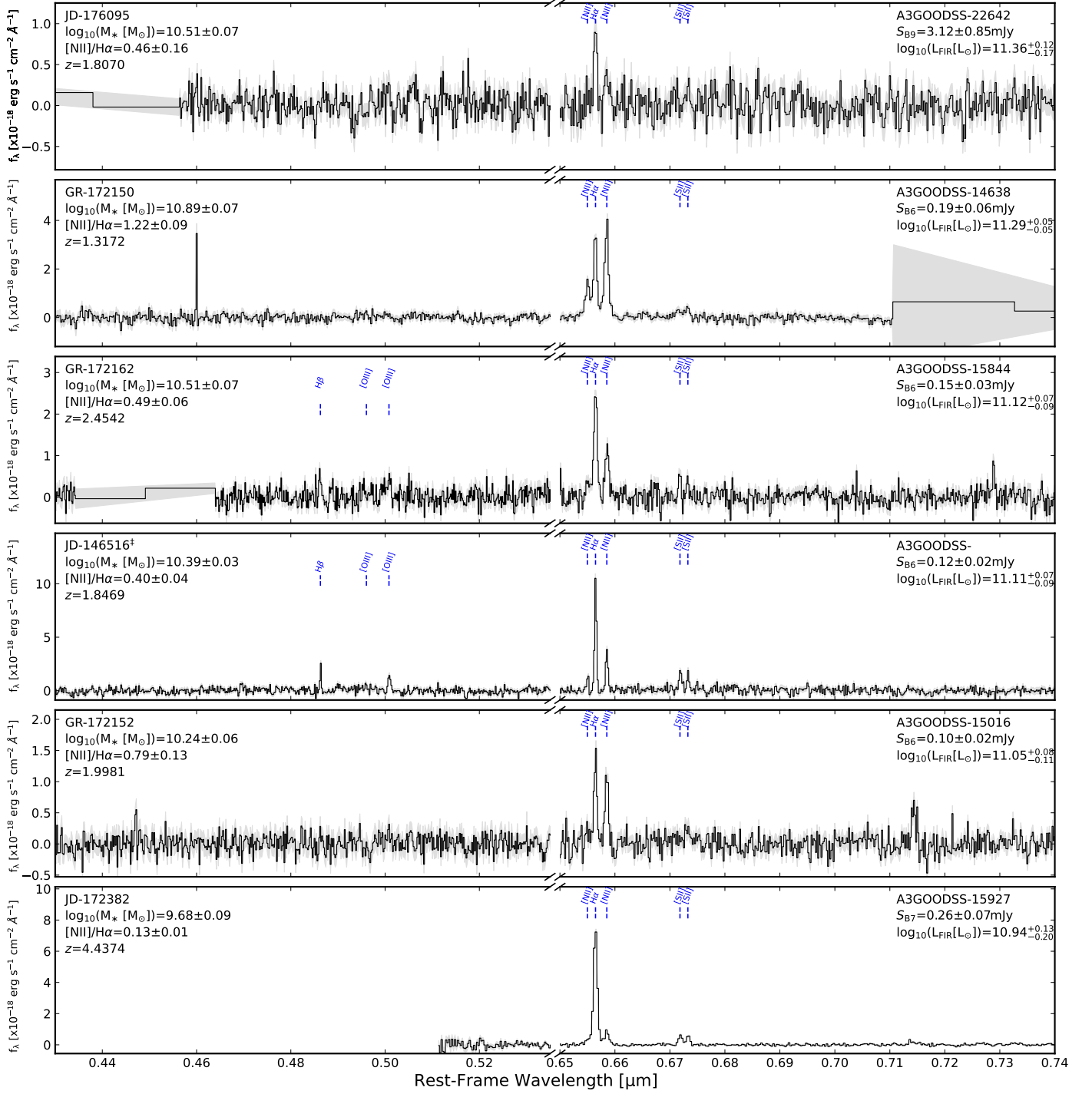


Fig. D.7: Continued...